Ground and excited state charmonium production in p+p collisions at sqrt[s]=200 GeV

A. Adare *et al.* (PHENIX Collaboration)

Phys. Rev. D **85**, 092004 — Published 9 May 2012

DOI: 10.1103/PhysRevD.85.092004

Ground and excited state charmonium production in p+p collisions at $\sqrt{s} = 200$ GeV

A. Adare,[12] S. Afanasiev,[28] C. Aidala,[40] N.N. Ajitanand,[57] Y. Akiba,[51,52] H. Al-Bataineh,[46] J. Alexander,[57] A. Angerami,[13] K. Aoki,[33,51] N. Apadula,[58] L. Aphecetche,[59] Y. Aramaki,[11,51] J. Asai,[51] E.T. Atomssa,[34] R. Averbeck,[58] T.C. Awes,[47] B. Azmoun,[6] V. Babintsev,[23] M. Bai,[5] G. Baksay,[19] L. Baksay,[19] A. Baldisseri,[15] K.N. Barish,[7] P.D. Barnes,[36,*] B. Bassalleck,[45] A.T. Basye,[1] S. Bathe,[7,52] S. Batsouli,[47] V. Baublis,[50] C. Baumann,[41] A. Bazilevsky,[6] S. Belikov,[6,*] R. Belmont,[63] R. Bennett,[58] A. Berdnikov,[54] Y. Berdnikov,[54] J.H. Bhom,[67] A.A. Bickley,[12] D.S. Blau,[32] J.G. Boissevain,[36] J.S. Bok,[67] H. Borel,[15] K. Boyle,[58] M.L. Brooks,[36] H. Buesching,[6] V. Bumazhnov,[23] G. Bunce,[6,52] S. Butsyk,[36] C.M. Camacho,[36] S. Campbell,[58] A. Caringi,[42] B.S. Chang,[67] W.C. Chang,[2] J.-L. Charvet,[15] C.-H. Chen,[58] S. Chernichenko,[23] C.Y. Chi,[13] M. Chiu,[6,24] I.J. Choi,[67] J.B. Choi,[9] R.K. Choudhury,[4] P. Christiansen,[38] T. Chujo,[62] P. Chung,[57] A. Churyn,[23] O. Chvala,[7] V. Cianciolo,[47] Z. Citron,[58] B.A. Cole,[13] Z. Conesa del Valle,[34] M. Connors,[58] P. Constantin,[36] M. Csanád,[17] T. Csörgő,[66] T. Dahms,[58] S. Dairaku,[33,51] I. Danchev,[63] K. Das,[20] A. Datta,[40] G. David,[6] M.K. Dayananda,[21] A. Denisov,[23] D. d'Enterria,[34] A. Deshpande,[52,58] E.J. Desmond,[6] K.V. Dharmawardane,[46] O. Dietzsch,[55] A. Dion,[27,58] M. Donadelli,[55] O. Drapier,[34] A. Drees,[58] K.A. Drees,[5] A.K. Dubey,[65] J.M. Durham,[58] A. Durum,[23] D. Dutta,[4] V. Dzhordzhadze,[7] L. D'Orazio,[39] S. Edwards,[20] Y.V. Efremenko,[47] F. Ellinghaus,[12] T. Engelmore,[13] A. Enokizono,[35,47] H. En'yo,[51,52] S. Esumi,[62] K.O. Eyser,[7] B. Fadem,[42] D.E. Fields,[45,52] M. Finger,[8] M. Finger, Jr.,[8] F. Fleuret,[34] S.L. Fokin,[32] Z. Fraenkel,[65,*] J.E. Frantz,[58] A. Franz,[6] A.D. Frawley,[20] K. Fujiwara,[51] Y. Fukao,[33,51] T. Fusayasu,[44] I. Garishvili,[60] A. Glenn,[12,35] H. Gong,[58] M. Gonin,[34] J. Gosset,[15] Y. Goto,[51,52] R. Granier de Cassagnac,[34] N. Grau,[13] S.V. Greene,[63] G. Grim,[36] M. Grosse Perdekamp,[24,52] T. Gunji,[11] H.-Å. Gustafsson,[38,*] A. Hadj Henni,[59] J.S. Haggerty,[6] K.I. Hahn,[18] H. Hamagaki,[11] J. Hamblen,[60] R. Han,[49] J. Hanks,[13] E.P. Hartouni,[35] K. Haruna,[22] E. Haslum,[38] R. Hayano,[11] X. He,[21] M. Heffner,[35] T.K. Hemmick,[58] T. Hester,[7] J.C. Hill,[27] M. Hohlmann,[19] W. Holzmann,[13,57] K. Homma,[22] B. Hong,[31] T. Horaguchi,[11,22,51,61] D. Hornback,[60] S. Huang,[63] T. Ichihara,[51,52] R. Ichimiya,[51] H. Iinuma,[33,51] Y. Ikeda,[62] K. Imai,[33,51] J. Imrek,[16] M. Inaba,[62] D. Isenhower,[1] M. Ishihara,[51] T. Isobe,[11,51] M. Issah,[57,63] A. Isupov,[28] D. Ivanischev,[50] Y. Iwanaga,[22] B.V. Jacak,[58,†] J. Jia,[6,13,57] X. Jiang,[36] J. Jin,[13] B.M. Johnson,[6] T. Jones,[1] K.S. Joo,[43] D. Jouan,[48] D.S. Jumper,[1] F. Kajihara,[11] S. Kametani,[51] N. Kamihara,[52] J. Kamin,[58] J.H. Kang,[67] J. Kapustinsky,[36] K. Karatsu,[33,51] M. Kasai,[51,53] D. Kawall,[40,52] M. Kawashima,[51,53] A.V. Kazantsev,[32] T. Kempel,[27] A. Khanzadeev,[50] K.M. Kijima,[22] J. Kikuchi,[64] A. Kim,[18] B.I. Kim,[31] D.H. Kim,[43] D.J. Kim,[29,67] E. Kim,[56] E.J. Kim,[9] S.H. Kim,[67] Y.-J. Kim,[24] E. Kinney,[12] K. Kiriluk,[12] Á. Kiss,[17] E. Kistenev,[6] J. Klay,[35] C. Klein-Boesing,[41] D. Kleinjan,[7] L. Kochenda,[50] B. Komkov,[50] M. Konno,[62] J. Koster,[24] A. Kozlov,[65] A. Král,[14] A. Kravitz,[13] G.J. Kunde,[36] K. Kurita,[51,53] M. Kurosawa,[51] M.J. Kweon,[31] Y. Kwon,[60,67] G.S. Kyle,[46] R. Lacey,[57] Y.S. Lai,[13] J.G. Lajoie,[27] D. Layton,[24] A. Lebedev,[27] D.M. Lee,[36] J. Lee,[18] K.B. Lee,[31] K.S. Lee,[31] T. Lee,[56] M.J. Leitch,[36] M.A.L. Leite,[55] B. Lenzi,[55] X. Li,[10] P. Lichtenwalner,[42] P. Liebing,[52] L.A. Linden Levy,[12] T. Liška,[14] A. Litvinenko,[28] H. Liu,[36,46] M.X. Liu,[36] B. Love,[63] D. Lynch,[6] C.F. Maguire,[63] Y.I. Makdisi,[5] A. Malakhov,[28] M.D. Malik,[45] V.I. Manko,[32] E. Mannel,[13] Y. Mao,[49,51] L. Mašek,[8,26] H. Masui,[62] F. Matathias,[13] M. McCumber,[58] P.L. McGaughey,[36] N. Means,[58] B. Meredith,[24] Y. Miake,[62] T. Mibe,[30] A.C. Mignerey,[39] P. Mikeš,[26] K. Miki,[51,62] A. Milov,[6] M. Mishra,[3] J.T. Mitchell,[6] A.K. Mohanty,[4] H.J. Moon,[43] Y. Morino,[11] A. Morreale,[7] D.P. Morrison,[6] T.V. Moukhanova,[32] D. Mukhopadhyay,[63] T. Murakami,[33] J. Murata,[51,53] S. Nagamiya,[30] J.L. Nagle,[12] M. Naglis,[65] M.I. Nagy,[17,66] I. Nakagawa,[51,52] Y. Nakamiya,[22] K.R. Nakamura,[33,51] T. Nakamura,[22,51] K. Nakano,[51,61] S. Nam,[18] J. Newby,[35] M. Nguyen,[58] M. Nihashi,[22] T. Niita,[62] R. Nouicer,[6] A.S. Nyanin,[32] C. Oakley,[21] E. O'Brien,[6] S.X. Oda,[11] C.A. Ogilvie,[27] M. Oka,[62] K. Okada,[52] Y. Onuki,[51] A. Oskarsson,[38] M. Ouchida,[22,51] K. Ozawa,[11] R. Pak,[6] A.P.T. Palounek,[36] V. Pantuev,[25,58] V. Papavassiliou,[46] I.H. Park,[18] J. Park,[56] S.K. Park,[31] W.J. Park,[31] S.F. Pate,[46] H. Pei,[27] J.-C. Peng,[24] H. Pereira,[15] V. Peresedov,[28] D.Yu. Peressounko,[32] R. Petti,[58] C. Pinkenburg,[6] R.P. Pisani,[6] M. Proissl,[58] M.L. Purschke,[6] A.K. Purwar,[36] H. Qu,[21] J. Rak,[29,45] A. Rakotozafindrabe,[34] I. Ravinovich,[65] K.F. Read,[47,60] S. Rembeczki,[19] K. Reygers,[41] V. Riabov,[50] Y. Riabov,[50] E. Richardson,[39] D. Roach,[63] G. Roche,[37] S.D. Rolnick,[7] M. Rosati,[27] C.A. Rosen,[12] S.S.E. Rosendahl,[38] P. Rosnet,[37] P. Rukoyatkin,[28] P. Ružička,[26] V.L. Rykov,[51] B. Sahlmueller,[41] N. Saito,[30,33,51,52] T. Sakaguchi,[6] S. Sakai,[62] K. Sakashita,[51,61] V. Samsonov,[50] S. Sano,[11,64] T. Sato,[62] S. Sawada,[30] K. Sedgwick,[7] J. Seele,[12] R. Seidl,[24,52] A.Yu. Semenov,[27] V. Semenov,[23] R. Seto,[7] D. Sharma,[65] I. Shein,[23] T.-A. Shibata,[51,61] K. Shigaki,[22] M. Shimomura,[62] K. Shoji,[33,51] P. Shukla,[4] A. Sickles,[6] C.L. Silva,[27,55] D. Silvermyr,[47] C. Silvestre,[15] K.S. Sim,[31] B.K. Singh,[3] C.P. Singh,[3] V. Singh,[3] M. Slunečka,[8] A. Soldatov,[23] R.A. Soltz,[35] W.E. Sondheim,[36] S.P. Sorensen,[60] I.V. Sourikova,[6] F. Staley,[15] P.W. Stankus,[47] E. Stenlund,[38] M. Stepanov,[46] A. Ster,[66] S.P. Stoll,[6] T. Sugitate,[22] C. Suire,[48] A. Sukhanov,[6] J. Sziklai,[66] E.M. Takagui,[55] A. Taketani,[51,52] R. Tanabe,[62]

Y. Tanaka,[44] S. Taneja,[58] K. Tanida,[33,51,52,56] M.J. Tannenbaum,[6] S. Tarafdar,[3] A. Taranenko,[57] P. Tarján,[16] H. Themann,[58] D. Thomas,[1] T.L. Thomas,[45] M. Togawa,[33,51,52] A. Toia,[58] L. Tomášek,[26] Y. Tomita,[62] H. Torii,[22,51] R.S. Towell,[1] V-N. Tram,[34] I. Tserruya,[65] Y. Tsuchimoto,[22] C. Vale,[6,27] H. Valle,[63] H.W. van Hecke,[36] E. Vazquez-Zambrano,[13] A. Veicht,[24] J. Velkovska,[63] R. Vértesi,[16,66] A.A. Vinogradov,[32] M. Virius,[14] V. Vrba,[26] E. Vznuzdaev,[50] X.R. Wang,[46] D. Watanabe,[22] K. Watanabe,[62] Y. Watanabe,[51,52] F. Wei,[27] R. Wei,[57] J. Wessels,[41] S.N. White,[6] D. Winter,[13] C.L. Woody,[6] R.M. Wright,[1] M. Wysocki,[12] W. Xie,[52] Y.L. Yamaguchi,[11,64] K. Yamaura,[22] R. Yang,[24] A. Yanovich,[23] J. Ying,[21] S. Yokkaichi,[51,52] Z. You,[49] G.R. Young,[47] I. Younus,[45] I.E. Yushmanov,[32] W.A. Zajc,[13] O. Zaudtke,[41] C. Zhang,[47] S. Zhou,[10] and L. Zolin[28]

(PHENIX Collaboration)

[1]*Abilene Christian University, Abilene, Texas 79699, USA*
[2]*Institute of Physics, Academia Sinica, Taipei 11529, Taiwan*
[3]*Department of Physics, Banaras Hindu University, Varanasi 221005, India*
[4]*Bhabha Atomic Research Centre, Bombay 400 085, India*
[5]*Collider-Accelerator Department, Brookhaven National Laboratory, Upton, New York 11973-5000, USA*
[6]*Physics Department, Brookhaven National Laboratory, Upton, New York 11973-5000, USA*
[7]*University of California - Riverside, Riverside, California 92521, USA*
[8]*Charles University, Ovocný trh 5, Praha 1, 116 36, Prague, Czech Republic*
[9]*Chonbuk National University, Jeonju, 561-756, Korea*
[10]*Science and Technology on Nuclear Data Laboratory, China Institute of Atomic Energy, Beijing 102413, P. R. China*
[11]*Center for Nuclear Study, Graduate School of Science, University of Tokyo, 7-3-1 Hongo, Bunkyo, Tokyo 113-0033, Japan*
[12]*University of Colorado, Boulder, Colorado 80309, USA*
[13]*Columbia University, New York, New York 10027 and Nevis Laboratories, Irvington, New York 10533, USA*
[14]*Czech Technical University, Zikova 4, 166 36 Prague 6, Czech Republic*
[15]*Dapnia, CEA Saclay, F-91191, Gif-sur-Yvette, France*
[16]*Debrecen University, H-4010 Debrecen, Egyetem tér 1, Hungary*
[17]*ELTE, Eötvös Loránd University, H - 1117 Budapest, Pázmány P. s. 1/A, Hungary*
[18]*Ewha Womans University, Seoul 120-750, Korea*
[19]*Florida Institute of Technology, Melbourne, Florida 32901, USA*
[20]*Florida State University, Tallahassee, Florida 32306, USA*
[21]*Georgia State University, Atlanta, Georgia 30303, USA*
[22]*Hiroshima University, Kagamiyama, Higashi-Hiroshima 739-8526, Japan*
[23]*IHEP Protvino, State Research Center of Russian Federation, Institute for High Energy Physics, Protvino, 142281, Russia*
[24]*University of Illinois at Urbana-Champaign, Urbana, Illinois 61801, USA*
[25]*Institute for Nuclear Research of the Russian Academy of Sciences, prospekt 60-letiya Oktyabrya 7a, Moscow 117312, Russia*
[26]*Institute of Physics, Academy of Sciences of the Czech Republic, Na Slovance 2, 182 21 Prague 8, Czech Republic*
[27]*Iowa State University, Ames, Iowa 50011, USA*
[28]*Joint Institute for Nuclear Research, 141980 Dubna, Moscow Region, Russia*
[29]*Helsinki Institute of Physics and University of Jyväskylä, P.O.Box 35, FI-40014 Jyväskylä, Finland*
[30]*KEK, High Energy Accelerator Research Organization, Tsukuba, Ibaraki 305-0801, Japan*
[31]*Korea University, Seoul, 136-701, Korea*
[32]*Russian Research Center "Kurchatov Institute", Moscow, 123098 Russia*
[33]*Kyoto University, Kyoto 606-8502, Japan*
[34]*Laboratoire Leprince-Ringuet, Ecole Polytechnique, CNRS-IN2P3, Route de Saclay, F-91128, Palaiseau, France*
[35]*Lawrence Livermore National Laboratory, Livermore, California 94550, USA*
[36]*Los Alamos National Laboratory, Los Alamos, New Mexico 87545, USA*
[37]*LPC, Université Blaise Pascal, CNRS-IN2P3, Clermont-Fd, 63177 Aubiere Cedex, France*
[38]*Department of Physics, Lund University, Box 118, SE-221 00 Lund, Sweden*
[39]*University of Maryland, College Park, Maryland 20742, USA*
[40]*Department of Physics, University of Massachusetts, Amherst, Massachusetts 01003-9337, USA*
[41]*Institut fur Kernphysik, University of Muenster, D-48149 Muenster, Germany*
[42]*Muhlenberg College, Allentown, Pennsylvania 18104-5586, USA*
[43]*Myongji University, Yongin, Kyonggido 449-728, Korea*
[44]*Nagasaki Institute of Applied Science, Nagasaki-shi, Nagasaki 851-0193, Japan*
[45]*University of New Mexico, Albuquerque, New Mexico 87131, USA*
[46]*New Mexico State University, Las Cruces, New Mexico 88003, USA*
[47]*Oak Ridge National Laboratory, Oak Ridge, Tennessee 37831, USA*
[48]*IPN-Orsay, Universite Paris Sud, CNRS-IN2P3, BP1, F-91406, Orsay, France*
[49]*Peking University, Beijing 100871, P. R. China*
[50]*PNPI, Petersburg Nuclear Physics Institute, Gatchina, Leningrad region, 188300, Russia*
[51]*RIKEN Nishina Center for Accelerator-Based Science, Wako, Saitama 351-0198, Japan*
[52]*RIKEN BNL Research Center, Brookhaven National Laboratory, Upton, New York 11973-5000, USA*
[53]*Physics Department, Rikkyo University, 3-34-1 Nishi-Ikebukuro, Toshima, Tokyo 171-8501, Japan*

[54]Saint Petersburg State Polytechnic University, St. Petersburg, 195251 Russia
[55]Universidade de São Paulo, Instituto de Física, Caixa Postal 66318, São Paulo CEP05315-970, Brazil
[56]Seoul National University, Seoul, Korea
[57]Chemistry Department, Stony Brook University, SUNY, Stony Brook, New York 11794-3400, USA
[58]Department of Physics and Astronomy, Stony Brook University, SUNY, Stony Brook, New York 11794-3400, USA
[59]SUBATECH (Ecole des Mines de Nantes, CNRS-IN2P3, Université de Nantes) BP 20722 - 44307, Nantes, France
[60]University of Tennessee, Knoxville, Tennessee 37996, USA
[61]Department of Physics, Tokyo Institute of Technology, Oh-okayama, Meguro, Tokyo 152-8551, Japan
[62]Institute of Physics, University of Tsukuba, Tsukuba, Ibaraki 305, Japan
[63]Vanderbilt University, Nashville, Tennessee 37235, USA
[64]Waseda University, Advanced Research Institute for Science and Engineering, 17 Kikui-cho, Shinjuku-ku, Tokyo 162-0044, Japan
[65]Weizmann Institute, Rehovot 76100, Israel
[66]Institute for Particle and Nuclear Physics, Wigner Research Centre for Physics, Hungarian Academy of Sciences (Wigner RCP, RMKI) H-1525 Budapest 114, POBox 49, Budapest, Hungary
[67]Yonsei University, IPAP, Seoul 120-749, Korea

We report on charmonium measurements [J/ψ (1S), ψ' (2S), and χ_c (1P)] in p+p collisions at $\sqrt{s} = 200$ GeV. We find that the fraction of J/ψ coming from the feed-down decay of ψ' and χ_c in the midrapidity region ($|y| < 0.35$) is $9.6 \pm 2.4\%$ and $32 \pm 9\%$, respectively. We also present the p_T and rapidity dependencies of the J/ψ yield measured via dielectron decay at midrapidity ($|y| < 0.35$) and via dimuon decay at forward rapidity ($1.2 < |y| < 2.2$). The statistical precision greatly exceeds that reported in our previous publication [Phys. Rev. Lett. **98**, 232002 (2007)]. The new results are compared with other experiments and discussed in the context of current charmonium production models.

PACS numbers: 13.85.Ni, 13.20.Fc, 14.40.Gx, 25.75.Dw

I. INTRODUCTION

Since its discovery, charmonium (bound $c\bar{c}$ states) has offered a powerful tool to investigate many aspects of QCD, including the distribution of partons in protons and nuclei at large momentum transfer. Charm quarks are predominantly produced in initial gluon interactions at $\sqrt{s} = 200$ GeV; therefore, they are sensitive to the gluon distribution in the nucleon and its modification in the nucleus. Color screening of the $c\bar{c}$ state in quark gluon plasma makes charmonium dissociation an important signature for the formation of a deconfined state of matter in A+A collisions [1, 2]. However, such studies rely on an accurate understanding of charmonium production in p+p collisions, which is the goal of the present work.

The cross section for $c\bar{c}$ production predicted from pQCD calculations agrees within a factor of two with PHENIX data [3, 4]. However, the hadronization step which forms the bound state is a nonperturbative process and is not well understood. A variety of schemes have been proposed, some of the most common being the Color Evaporation Model (CEM), the Color Singlet Model (CSM) and nonrelativistic quantum chromodynamics (NRQCD), which is also known as the Color Octet Model (COM). In this paper we review these models briefly and compare calculated results to our data.

In the CEM [5, 6] the bound-state production mechanism is insensitive to the $c\bar{c}$ quantum numbers. A $c\bar{c}$ pair is produced as long as the center of mass energy of the pair, $\sqrt{\hat{s}}$, exceeds the mass of two charm quarks but is less than the mass of two open charm mesons. Charmonium states are then color neutralized during the hadronization process by soft gluon emission. The yield of different charmonium states is a fixed fraction $\mathcal{F}$ of the integrated pQCD $c\bar{c}$ cross section, where $\mathcal{F}$ is a universal value determined from experiments. Hence, ratios of the yields of different charmonium states is momentum and energy independent.

In the CSM [7] the production amplitude of on-shell $c\bar{c}$ pairs is projected onto ${}^{2S+1}L_J$ angular momentum states, accounting for the J/ψ and the ψ' as ${}^3S_1$ and the χ_c states as ${}^3P_{0,1,2}$. The model assumes that these charmonium states are formed in their final color singlet quantum number configuration. The production density matrix is coupled

*Deceased
†PHENIX Spokesperson: jacak@skipper.physics.sunysb.edu

to the wave function at the origin, which is determined from potential models. The only empirical parameters in the entire calculation are the leptonic decay width and the charmonium mass used in the potential model.

NRQCD allows for the production of both color singlet and color octet $c\bar{c}$ states. Color octet states emit one or more gluons during hadronization in order to neutralize their color. The production amplitude is expanded in powers of both the strong coupling, α_S, and the velocity, ν, of the heavy quarks relative to the $c\bar{c}$ pair. The expansion in ν assumes that the heavy quark is nonrelativistic[1]. As in the CSM, the production amplitudes are projected onto $^{2S+1}L_J$ states. Since the potential model can only be applied to the color singlet state, a long range nonperturbative matrix element for each quarkonium state is taken from fits to experimental data. The earliest such matrix parametrization [8] was tuned with J/ψ and ψ' cross sections observed in CDF ($\sqrt{s} = 1.8$ TeV) [9] which indicated that while P-wave charmonium (χ_c) has no important color octet state contributions, S-wave charmonium (direct J/ψ and ψ') production is largely through color octet channels. Therefore, this model is sometimes simply referred to as the Color Octet Model (COM).

Each model has its strengths and weaknesses. The CEM is able to reasonably describe quarkonia yields observed in many experiments, but has no predictive power for $c\bar{c}$ polarization. Cross sections calculated using the CSM grossly underestimate the yields observed in CDF [9] and the previous PHENIX [10] measurements. Recent next-to-leading-order (NLO) [11–13] and next-to-next-to-leading-order (NNLO) [14–17] calculations for the color singlet states resulted in significant modifications of the predicted charmonium yields and polarization, but still do not agree with experiment. NRQCD calculations tuned with J/ψ and ψ' p_T spectra from CDF were able to qualitatively describe the first PHENIX J/ψ cross section and polarization results [18] albeit within large experimental uncertainties, but failed to describe the J/ψ and ψ' polarization observed in CDF [19] (see [15] for a recent review). Recent NRQCD calculations [20] include color singlet and color octet NLO short range terms along with a long-range matrix parametrization from experimental hadroproduction [21] and photoproduction [22, 23] of J/ψ mesons. A similar study was performed using CDF data with consistent results [24]. However, the NLO terms for the color octet [25] have only small corrections compared to the leading-order (LO) terms and the calculations still disagree with the J/ψ polarization measured by CDF.

One of the complications in the J/ψ total cross section and polarization calculations (observables where experimental tests are readily available) is the contribution from the decays of excited charmonium states, primarily ψ', χ_{c1} and χ_{c2}. In addition, the J/ψ suppression observed in heavy ion collisions cannot be completely understood without a knowledge of the feed-down fraction of excited charmonium state decays to the J/ψ. This is particularly true under the assumption that the suppression is due to the disassociation of charmonium in the high temperature quark-gluon plasma, since lattice calculations [2] indicate that the melting points of the χ_c and ψ' states are lower than that of the J/ψ. In this work the feed-down fractions to the J/ψ from excited charmonium states are measured, since they can be determined more precisely than production cross sections as various systematic uncertainties cancel.

The PHENIX experiment measures quarkonia via dilepton decays over a broad p_T and rapidity range. Furthermore, PHENIX can detect photons from χ_c radiative decays using electromagnetic calorimeters at midrapidity. This paper reports the feed-down fraction of J/ψ from ψ' and χ_c decays at midrapidity in p+p collisions at $\sqrt{s} = 200$ GeV. To accomplish this, we measured the ψ' to J/ψ yield ratio in the dielectron channel and fully reconstructed the $p+p \rightarrow \chi_c \rightarrow J/\psi \ + \gamma \rightarrow e^+e^- + \gamma$ decay. New J/ψ differential cross section measurements at mid and forward rapidities using the increased luminosity obtained in 2006 and 2008 are also presented. These provide more accurate measurements than previously published [10], particularly for the J/ψ differential cross section at high p_T. The results also provide a baseline for the study of J/ψ suppression in d+Au [26] and Au+Au [27, 28] collisions by PHENIX.

Systematic uncertainties throughout this article are classified according to the type of correlation among the experimental uncertainties. Type A systematic uncertainties are point-to-point uncorrelated, similar to statistical uncertainties, since the points fluctuate randomly with respect to one another. Type B systematic uncertainties are point-to-point correlated. The points fluctuate coherently with respect to each other, accounting for the uncertainty in the nth-order derivative of the measured spectrum, in most cases the slope. Global, or type C, systematic uncertainties are those where all points fluctuate in the same direction by the same fractional amount.

The remainder of the article is arranged as follows. An introduction to the PHENIX detector, a description of the data sample, and a description of the lepton identification method are given in Sec. II. The analysis is described in three sections: midrapidity J/ψ and ψ' dielectron measurements in the PHENIX central arms are in Sec. III; direct χ_c feed-down measurement in the central arms is given in Sec. IV; and forward rapidity J/ψ measurements in the muon arms are described in Sec. V. The results are compared to those from other experiments and to current theoretical calculations in Sec. VI.

[1] Potential model calculations indicate the velocity of charm(bottom) is $\sim 0.23(0.1)c$.

II. EXPERIMENTAL APPARATUS AND THE DATA SET

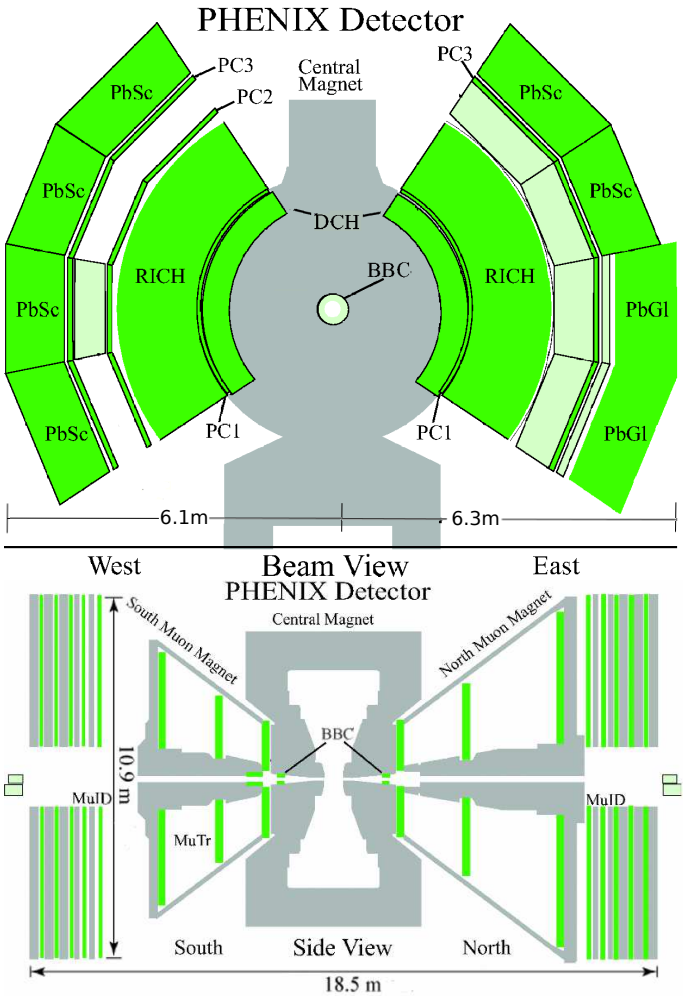

FIG. 1: (Color online) PHENIX apparatus with emphasis on the subsystems used in lepton and photon detection.

Figure 1 shows the PHENIX detector [29], which comprises four spectrometer arms plus detectors for event characterization and triggering. The $\hat{z}$ axis lies along the beam line with the origin at the nominal center of the detector and points toward the north arm. The $\hat{x}$ axis points towards the west central arm. The two central arms detect electrons, photons and hadrons in the range $|\eta| < 0.35$; each arm covers $\Delta\phi = \pi/2$ radians in azimuth. The two forward muon arms detect muons in the range $-2.2 < \eta < -1.2$ and $1.2 < \eta < 2.4$ with full azimuthal coverage. The rapidity dependence of observables is generally measured over the full acceptance of the muon arms, but p_T -dependence studies are constrained to the symmetric range $1.2 < |y| < 2.2$ in J/ψ rapidity, allowing the forward and backward rapidity measurements to be averaged. It is clear from Fig. 1 that the acceptance and detector technologies for dimuons and dielectrons are very different in PHENIX, necessitating development of different analysis approaches.

Charged particle tracks are reconstructed in the central arms using the Drift Chambers (DCH) and Pad Chambers (primarily PC1 and PC3) [30, 31]. Electron candidates require at least one phototube above pedestal in the

Ring Imaging Čerenkov detector (RICH)[2], within an annulus $3.4 < R_{\rm ring}[{\rm cm}] < 8.4$ around the projected track position. In addition, the electron candidate is required to be associated with an energy cluster in the Electromagnetic Calorimeter. Clusters must lie within $4\sigma_{\rm position}$ of the projected track position, and within $4\sigma_{\rm energy}$ of the expected energy/momentum ratio. The σs characterize the position and energy resolution of the EMCal, which comprises 6 Pb-Scintillator (PbSc) and 2 Pb-Glass (PbGl) sectors, each calibrated separately. The material between the center of the detector and the EMCal, corresponds to a radiation length of 0.4%, minimizing the production of $\gamma \to e^+e^-$ conversions. The granularity of the PHENIX detectors was driven by the very high multiplicity environment of Au+Au collisions. Consequently, the occupancy in p+p collisions is very low, and the relatively loose association requirement of $4\sigma_{\rm position}$ provides excellent hadron rejection. Based on the p_T range of decay electrons from J/ψ observed in real data and simulations, a minimum p_T of 500 MeV/c was required for each electron candidate.

Each forward muon arm [32] contains a hadron absorber, three stations of cathode strip chambers for particle tracking (MuTr), and a Muon Identifier (MuID). The hadron absorber has two parts: a 20 cm thick conical shaped copper absorber and 60 cm of magnet iron. The MuTr is installed inside the eight-sided conical magnet. The MuID comprises five steel hadron absorbers interleaved with six panels of vertical and horizontal Iarocci tubes. A muon needs 2.5 (2.3) GeV/c longitudinal momentum to reach the furthest downstream Iarocci tube in the MuID north (south). Tracks reconstructed in the MuTr are identified as muons if they match a "road" formed by hits in the MuID, within 2.5σ of the angular resolution. The associated road is required to include at least one hit in the downstream-most MuID plane. Additional cuts include $\chi^2 < 23$ for the reconstructed track, $\chi^2 < 7$ for the dimuon projection to the collision vertex, and a minimum longitudinal momentum cut ensuring that the muon will reach the last gap of the MuID.

Beam interactions were selected with a minimum-bias (MB) trigger that required at least one hit per beam crossing in each of the two beam-beam counters (BBC) placed at $3.0 < |\eta| < 3.9$. Each BBC has an array of Čerenkov detectors, and measures the arrival time, as well as multiplicity, of particles [33]. Studies using Vernier scans (also called van der Meer scans) [34] conclude that this MB trigger accepts a cross section of $\sigma_{\rm BBC} = 23.0 \pm 2.2$ mb, representing 55 $\pm$5% of the 42 $\pm$ 3 mb p+p inelastic cross section at $\sqrt{s} = 200$ GeV.

Dedicated triggers were used to select events with at least one electron or two muon candidates. An EMCal RICH Trigger (ERT) required a minimum energy in any 2×2 group of EMCal towers, corresponding to $\Delta\eta\times\Delta\phi = 0.02\times0.02$ rad, plus associated hits in the RICH. The minimum EMCal energy requirement was 400 MeV for the first half of the data-taking period and 600 MeV for the second half, when the instantaneous luminosity was high. Electron data used in this analysis required the ERT in coincidence with the MB trigger. Another trigger selected events with two muon candidates in a single muon arm, using the MuID. The trigger logic for a muon candidate required a "road" of fired Iarocci tubes in at least four planes, including the most downstream plane relative to the collision point. The event sample used in the dimuon analysis also required a valid MB trigger in coincidence with the MuID trigger.

The MB trigger has a sensitivity that depends upon the particle multiplicity in the collision. The MB condition is more likely to be fulfilled by high multiplicity events. Consequently, a hard process, such as one producing a J/ψ or a high energy π^0, will fire the MB trigger with a higher probability than, for example, a diffractive process. This implies a different MB efficiency for the event sample used in the current analysis. This effect was investigated using a data sample requiring the ERT trigger, but with no MB requirement. Given enough events one could, in principle, use the J/ψ yield in an ERT-only triggered sample (after correction for any prescale factors) to estimate the MB coincidence requirement upon the yield. However, we did not have a sufficient number of ERT-only triggered events to make a statistically significant study of J/ψ yields with and without satisfying the MB trigger. Since the relevant issue is the effect of a hard collision on the particle multiplicity, an alternate approach was taken. Several variants of the ERT trigger were implemented in parallel, with some requiring a high energy shower in the EMCal without a corresponding hit in the RICH (i.e. photon triggers). We counted $\pi^0 \to \gamma\gamma$ decays with a p_T greater than 3 GeV/c using the photon trigger; in 79 ± 2% of such events the MB trigger fired, indicating $\varepsilon_{\rm inel} = 79 \pm 2$%. No dependence of $\varepsilon_{\rm inel}$ on the p_T of the measured π^0 decays was found over the range 0-10 GeV/c . More details can be found in [35]. This factor is included as a correction in all cross section calculations requiring the MB trigger.

The collision point along the beam direction was determined with a resolution of 1.5 cm by using the difference between the fastest time signals measured in the north and south BBC detectors. The collision point was required to be within $\pm$30 cm of the nominal center of the detector to avoid backgrounds from the central magnet pole faces. In order to ensure uniform detector response in the dielectron analysis, data sets in which electron yields were more than three standard deviations away from the average in one or more of the EMCal sectors were discarded. For the dimuon analysis, data sets where the muon arm spectrometers were not fully operational were rejected.

The 2006 data sample used in the dielectron analysis corresponded to $N_{pp} = 143$ billion minimum bias events, or

[2] Corresponding to $\Delta\phi = 8$ mrad and $\Delta Z = 3$ cm.

an integrated luminosity of $\int \mathcal{L}dt = N_{pp}/\sigma_{\rm BBC} = (6.2 \pm 0.6)$ pb^{-1}. The 2006 and 2008 data samples used for the muon analysis, corresponded to 215 billion minimum bias events, or a luminosity of (9.3 ± 0.9) pb^{-1}.

III. J/ψ AND ψ' ANALYSIS IN THE MIDRAPIDITY REGION

The procedure for analyzing the J/ψ and $\psi' \to e^+e^-$signal in the central arm detectors is described in this section. The overall procedure to select dielectrons, extract the charmonium signal, and determine combinatorial and correlated backgrounds is explained in III A. Studies of the central arm detector response to charmonium decays is the subject of Sec. III C. The final p_T and rapidity dependencies of the cross sections are calculated in Sec. III D, together with a summary of all systematic uncertainties mentioned throughout the text. Finally the $\psi'/(J/\psi)$ dielectron yield ratio is calculated in Sec. III E.

A. Dielectron decays of J/ψ and ψ' mesons in the midrapidity region

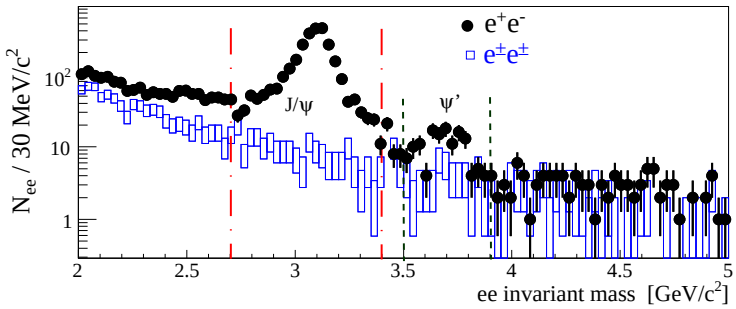

FIG. 2: (Color online) Invariant mass distribution of unlike-sign (closed circles) and like-sign (open boxes) dielectrons in the J/ψ and ψ' region. Dash-dotted (dashed) lines represent the mass range used to count J/ψ (ψ') decays.

The invariant mass was calculated for all electron pairs in which one electron of the pair geometrically matched the position of a fired ERT segment. This requirement was necessary because simulated J/ψ and ψ' decays were used to estimate the ERT efficiency. J/ψ and ψ' decays are clearly visible as peaks in the unlike sign invariant mass distribution in Fig. 2. The primary sources of physically correlated unlike-sign pairs (e^+e^-) are quarkonia decays, open $c\bar{c}$ and $b\bar{b}$ pairs, Drell-Yan pairs, and unlike-sign electrons from decays of particles within the same jet. According to studies performed in [36] using Monte-Carlo simulation and real data, the primary sources of like-sign pairs ($e^+e^+ + e^-e^-$) are combinatorial background (which is uncorrelated), and correlated electrons from particle decays occurring in the same jet (mostly π^0 Dalitz decays). We use the like-sign dielectrons to subtract the combinatorial and a portion of the correlated background from the unlike-sign pair counts.

A challenge of the PHENIX dielectron analysis is that the lack of full azimuthal coverage results in acceptance differences for like-sign and unlike-sign pairs. In order to account for the different acceptances of e^- and e^+, the like-sign pair count was normalized to the geometric mean A, of the number of e^+e^+ (N_{++}) and e^-e^- pairs (N_{--})

$$A = \frac{2\sqrt{N_{++}N_{--}}}{N_{++} + N_{--}}. \quad (1)$$

There were 2,882 unlike-sign and 203 like-sign dielectrons in the J/ψ mass range ($2.7 < M_{ee}[\mathrm{GeV}/c^2] < 3.4$), giving a correlated signal of 2,679 $\pm$ 56 counts and a signal/background of 13. In the ψ' mass region ($3.5 < M_{ee}[\mathrm{GeV}/c^2] < 3.9$) there were 137 unlike-sign and 51 like-sign electron pairs corresponding to a signal of 86 $\pm$ 14 counts and signal/background of 1.7.

Given the low statistics in many of the p_T bins of the unlike-sign dielectron pairs (which we will refer to as "foreground") and the like-sign pairs ("background"), Poisson statistics precludes the use of a simple subtraction. The correlated yield and corresponding statistical uncertainties used in the cross section calculations were obtained assuming that the foreground and background distributions are independent. In each bin of p_T (or y), the foreground signal (μ_f) was obtained from the unlike-sign counts (f) in the charmonium mass range and the background (μ_b)

was obtained from the like-sign counts (b) in the same mass range (Fig. 2). The joint probability distribution for the correlated dielectron signal $s = \mu_f - \mu_b$ is

$$P(s,\mu_b) = \frac{\mu_b^b}{b!}\frac{\mu_b^f}{f!}e^{-2\mu_b}\left(1+\frac{s}{\mu_b}\right)^f e^{-s}. \tag{2}$$

We expand the term $\left(1+\frac{s}{\mu_b}\right)^f$:

$$\begin{aligned}\left(1+\frac{s}{\mu_b}\right)^f &= \sum_{k=0}^{f}\frac{f!}{(f-k)!k!}\left(\frac{s}{\mu_b}\right)^k \\ P(s,\mu_b) &= \sum_{k=0}^{f}\frac{\mu_b^{b+f-k}e^{-2\mu_b}}{b!(f-k)!}\frac{s^k e^{-s}}{k!}.\end{aligned} \tag{3}$$

Assuming no negative signal, the expression is summed over μ_b from 0 to ∞ using the normalization of the Γ distribution

$$\int_0^\infty dx x^{p-1}e^{-bx} = \frac{(p-1)!}{b^p} \tag{4}$$

and $b = 2$, $p - 1 = b + f - k$. We obtain finally,

$$P(s) = \sum_{k=0}^{f}\frac{(b+f-k)!}{b!(f-k)!}\frac{1}{2}\left(\frac{1}{2}\right)^{b+f-k}\frac{s^k e^{-s}}{k!} \tag{5}$$

which we use to find the most probable number of events in each bin of p_T as a function of the mass. The mean value $\langle s\rangle_P$ and standard deviation of $P(s)$ corresponds to the number of correlated dielectrons and statistical uncertainty in the chosen mass range and p_T. The number of dielectrons obtained in the J/ψ and ψ' mass regions are listed in Table I and II, respectively.

The number of charmonium decays is

$$N_\psi = \langle s\rangle_P \times f_\psi. \tag{6}$$

where f_ψ is the the fraction of charmonium decays in these correlated dielectrons. This fraction is estimated in Sec. III B.

B. Correlated background estimation

As previously mentioned, the correlated background comprises dielectrons coming from jets, open heavy flavor decays and Drell-Yan pairs. The jet contribution in the charmonium mass region is three orders of magnitude below the J/ψ and ψ' with a steeply falling mass spectrum [36] and will be ignored here; in any case it is largely removed by the like-sign subtraction. The Drell-Yan contribution was estimated using next-to-leading-order calculations [37]. Taking into account the detector acceptance, the fraction of the dielectron signal coming from Drell-Yan processes is 0.23 ± 0.03 % in the J/ψ mass region and 3.37 ± 0.40 % in the ψ' region. The open heavy flavor contributions are the major background to the correlated dielectron spectrum. In fact, they represent a significant fraction of the correlated dielectrons in the ψ' mass region. They will be estimated by two models as described below.

In order to untangle different contributions to the dielectron spectrum, a simulation was done for the three primary contributions to the mass spectrum: the J/ψ and ψ', Drell-Yan pairs and heavy quark pairs. The first step was to generate the initial correlated electron pair spectrum. The J/ψ and ψ' were generated by weighting their distributions in order to obtain the same p_T spectrum as seen in real data. The J/ψ radiative decay ($J/\psi \to e^+e^- + \gamma$), also called internal radiation, was introduced using the mass distribution estimated from QED calculations [38]. Drell-Yan pairs were generated according to the mass distribution obtained from NLO calculations.

TABLE I: Foreground, background counts in the J/ψ mass region, and the signal count and statistical error obtained from Eq. (5).

p_T [GeV/c]	e^+e^- counts	like-sign pairs	net count
0-0.25	93	2	91 ± 9
0.25-0.5	212	16	196 ± 15
0.5-0.75	326	23	303 ± 19
0.75-1	370	25	345 ± 20
1-1.25	384	18	366 ± 20
1.25-1.5	313	25	288 ± 18
1.5-1.75	265	23	242 ± 17
1.75-2	229	16	213 ± 16
2-2.25	170	13	157 ± 14
2.25-2.5	119	13	106 ± 11
2.5-2.75	103	8	95 ± 11
2.75-3	71	10	61 ± 9
3-3.25	52	2	50 ± 7
3.25-3.5	38	2	36 ± 6
3.5-3.75	25	0	25 ± 5
3.75-4	21	1	20 ± 5
4-4.25	15	2	$13^{+4.3}_{-4.2}$
4.25-4.5	8	0	$8^{+3.1}_{-3.0}$
4.5-4.75	12	0	$12^{+3.7}_{-3.6}$
4.75-5	10	1	$9^{+3.5}_{-3.4}$
5-6	27	3	$24^{+5.5}_{-5.6}$
6-7	11	0	11 ± 3.3
7-8	6	0	$6^{+2.8}_{-2.6}$
8-9	2	0	$2^{+2}_{-1.2}$

TABLE II: Foreground, background counts in the ψ' mass region, and the signal count and statistical error obtained from Eq. (5).

p_T [GeV/c]	e^+e^- counts	like-sign pairs	net count
0-1	33	9	24 ± 7
1-2	55	20	35 ± 9
2-3	27	12	15 ± 6
3-5	15	9	$6^{+5.5}_{-3.3}$
5-7	3	2	< 3.3 (90% CL)
0-5	137	51	86 ± 14

In order to make a conservative estimate and determine whether the result is model independent, the $c\bar{c}$ and $b\bar{b}$ mass distributions were obtained using two different methods:

(1) *Dielectron generator* – The semi-leptonic heavy flavor yield measured in [35, 39] was split into the $c\bar{c}$ ($d\sigma_{c\bar{c}}/dp_T$) and $b\bar{b}$ ($d\sigma_{b\bar{b}}/dp_T$) distributions according to the c/b ratio from fixed-order plus next-to-leading-log (FONLL) calculations [3] which agree with PHENIX and STAR measurements of open charm and bottom production [40, 41]. These yields were used as input for an electron Monte-Carlo generator with uniform rapidity distribution inside $|y| < 0.5$ and the measured vertex distribution. An electron and positron from the decay of a heavy quark pair were generated for each event. In this method the heavy quarks are assumed to have no angular correlation.

(2) PYTHIA – Hard scattering collisions were simulated using the PYTHIA [42] generator. Leading order pair creation sub-processes and next-to-leading-order flavor creation and gluon splitting sub-processes are all included in the heavy quark generation [43]. These sub-processes have different opening angles for the heavy quark pair, and the opening angle directly affects the shape of the mass and p_T distributions. The simulation used the CTEQ6M [44] parton distribution functions (PDF), a Gaussian k_T distribution of width 1.5 GeV/c, a charm quark mass of 1.5 GeV/c^2 and bottom quark mass of 4.8 GeV/c^2 . Variations of the k_T distribution and masses of the heavy quarks were included in the systematic uncertainties. The p_T dependence of electrons from $c\bar{c}$ and $b\bar{b}$ given by the simulation agrees with the PHENIX measurement of single electrons from heavy flavor decay [35].

The generated electron pairs from all sources were then used as input to a GEANT-3 [45] based detector Monte-Carlo calculation, which included effects such as bremsstrahlung of electrons when crossing detector material and air (external radiation). Simulated events were reconstructed and analyzed using the same criteria used for real data that

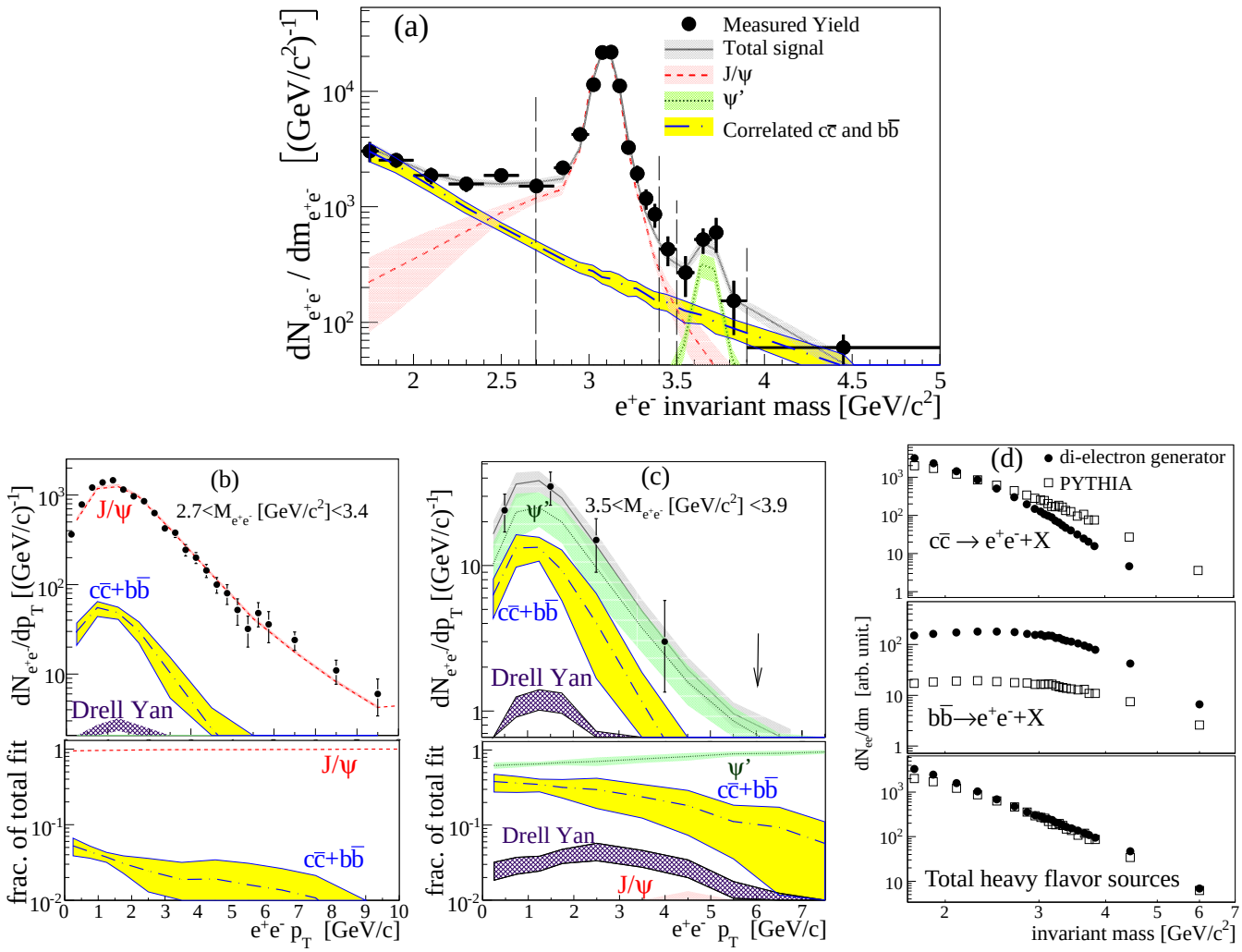

FIG. 3: (Color online) Correlated dielectron mass (a) and p_T distributions in the J/ψ (b) and ψ' (c) mass regions. Signal components were estimated by fitting to Eq. (A1) including simulated open heavy flavor, Drell Yan pairs, J/ψ and ψ' decays contributions. The $c\bar{c}$ and $b\bar{b}$ components were generated using PYTHIA [42] and a heavy flavor based dielectron generator described in the text. Bands correspond to the type A fitting uncertainties and the type B systematic uncertainty obtained when using the two different open heavy quark generators. Panel (d) shows the result after the fit for $c\bar{c}$, $b\bar{b}$ and total open heavy flavor components from each generator.

are reported in Sec. II and Sec. III A. These simulated data were then used to generate mass vs. p_T histograms for each electron pair source. More details will be given later in Sec. III C, including methods of estimating systematic uncertainties. These were fit to real data distributions to determine the relative contribution of each source, as described in Appendix A.

Figure 3 shows the results of the fit for the dielectron mass (a) and p_T (b,c) projections of the two-dimensional histogram. The heavy flavor contribution to the continuum obtained from the fit using the shapes from the dielectron generator and PYTHIA is shown in Fig. 3-d. When using the PYTHIA simulation, the presence of back-to-back correlated $c\bar{c}$ and $b\bar{b}$ pairs produced more high mass pairs per $c\bar{c}$ which then forced a smaller contribution from $b\bar{b}$. The fits performed using the two generators give very different normalizations for the open charm and the open bottom contributions. However, the two methods give very similar contributions for the sum which is well constrained by data. Thus lack of the knowledge of angular correlation in heavy flavor production does not affect the estimate of the total continuum contribution from open heavy flavor in the J/ψ and ψ' mass regions. The measurement of the $c\bar{c}$ and $b\bar{b}$ cross sections is not in the scope of this paper; a more detailed study can be found in [40, 41, 46]. Type A fit parameter uncertainties and the type B uncertainty obtained from the difference in results obtained using the two generators for the total heavy flavor contribution are summed in quadrature and shown as bands in Fig. 3. Values for the fraction of the charmonium signal (f_ψ) shown in Figs. 3-b and 3-c are used later in the yield calculation.

The fitted external and internal radiation contributions in the data indicate that the fraction of radiative decays of the J/ψ, where the undetected photon has energy larger than 100 MeV, is 9 ± 5 %. This is consistent with QED calculations which indicate that 10.4% of the dielectron decays from the J/ψ come from such radiative decays and a measurement of fully reconstructed $J/\psi \to e^+e^-\gamma$ performed by E760 [47] which gives 14.7 ± 2.2 %. The J/ψ mass peak around 3.096 GeV/c^2 has a Gaussian width from the fit of 53 ± 4 MeV after including a mass resolution in the MC of $(\delta M/M)$=1.71 $\pm$ 0.13 %. Because of the radiative tails, the mass range (2.7< M_{ee}[GeV/c^2] <3.4) contains a fraction $\varepsilon^{J/\psi}_{\rm mass} = 93.8 \pm 0.9\%$ of the J/ψ decays and the mass region (3.5< M_{ee}[GeV/c^2] <3.9) contains a fraction $\varepsilon^{\psi'}_{\rm mass} = 86 \pm 2\%$ of the ψ' decays; these corrections are included in the yield calculations.

Finally, the fractions of charmonium decays f_ψ used in Eq. (6) and shown in Figs. 3-b and 3-c, are multiplied by the number of correlated counts to obtain the number of charmonium decays.

C. Dielectron acceptance and efficiency studies

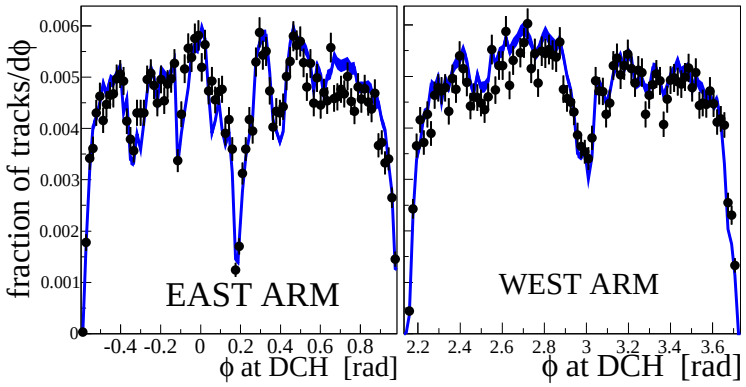

FIG. 4: (Color online) Simulated (solid line) and real data (points) single electron distributions in the ϕ coordinate of the drift chamber. Error bars correspond to statistical uncertainties.

The detector response to J/ψ and ψ' dielectron decays was studied using the GEANT3-based Monte-Carlo simulation. Malfunctioning detector channels were removed from the detector simulation and from the real data analysis. The geometric acceptance of the detector Monte-Carlo calculation was compared to that for real data using simulated π^0 decays. This channel is used because the majority of the electrons found in real data come from π^0 Dalitz decays and photons, which convert in the detector material. In this study, simulated electrons from π^0 decays were weighted to match the collision vertex and p_T distributions observed in the data. Figure 4 shows the simulated and real electron track distribution as a function of the azimuthal angle, ϕ, measured at the DCH radial location. The ratio between real and simulated track distributions $f_{\rm acc}\,(\phi_{\rm DCH}, z_{\rm DCH})$ is used later to estimate the systematic uncertainty of the J/ψ acceptance.

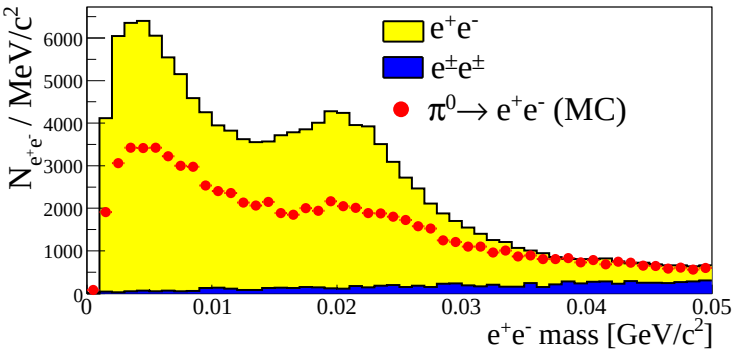

FIG. 5: (Color Online) Low mass dielectrons in real data. This sample was used to estimate the electron identification efficiency.

The electron identification efficiency was estimated using π^0 Dalitz decays and $\gamma \to e^+e^-$ conversions coming primarily from the beam pipe. The invariant mass of unlike sign pairs in the mass range of these decays is shown

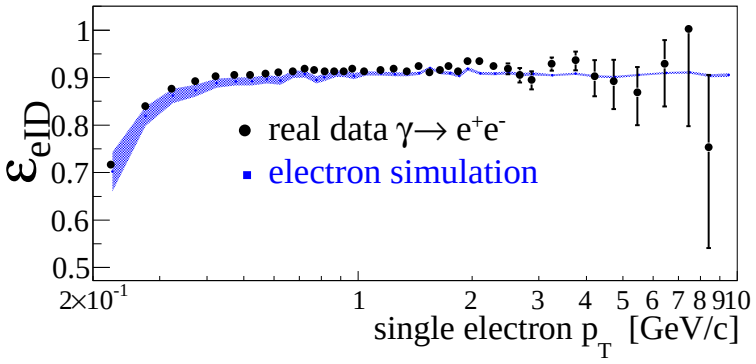

FIG. 6: (Color Online) Single electron identification efficiency estimated using photon conversions (Fig. 5) from real data (points) and the electron simulation (shaded area).

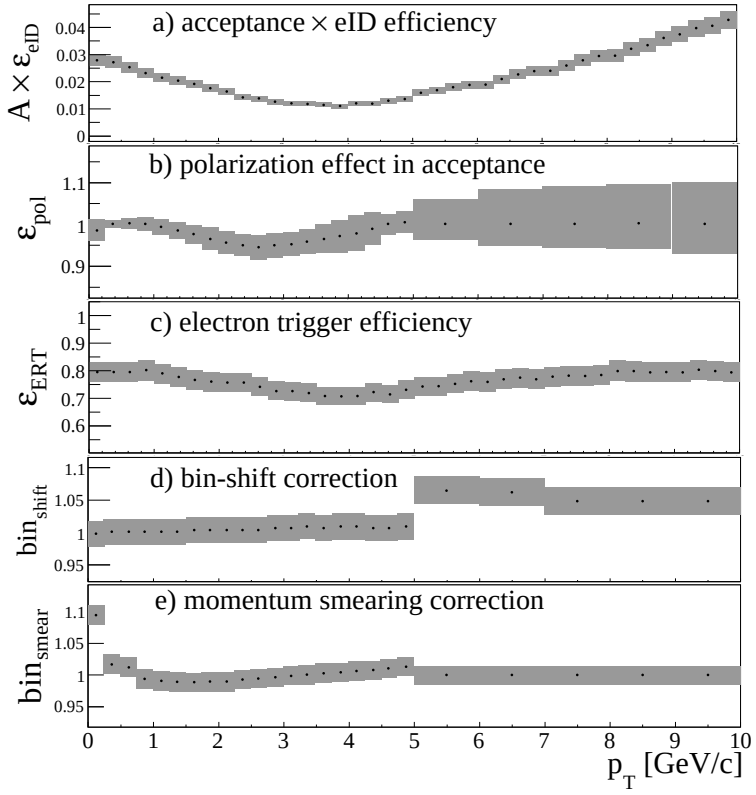

FIG. 7: Transverse momentum dependence of the detector performance and correction factors for dielectron decays of J/ψ mesons in $|y| < 0.5$. Shaded bands are the uncertainties of the estimates as described in the text.

in Fig. 5. The combinatorial background, determined from like-sign pairs, is negligible in this very low mass region. No electron identification criteria are applied in the sample. The Dalitz decays are dominant near zero mass whereas γ conversions are peaked at 20 MeV/c^2. This is because their primary source is in the beam pipe while the track reconstruction assumes that particles originate from the vertex and traverse the entire magnetic field. We assume all pairs above the combinatorial background in the mass region below 0.30 GeV/c^2 are true dielectrons. The electron identification efficiency was obtained from the fraction of dielectron conversions which survive the identification criteria are applied to both the electron and positron compared to the number of dielectron conversions obtained after requiring identification for only one electron or positron. The same procedure was repeated in the simulation. Figure 6 shows the electron identification efficiency as a function of the p_T of the electron in question. The difference in efficiency between simulation and data for electrons with $p_T > 0.5$ GeV/c was no larger than 0.8%, which translated to an overall type B uncertainty in the dielectron yield of 1.1%.

Simulated J/ψ dielectron decays were generated with uniform p_T and rapidity ($|y| < 0.5$) and the measured vertex

distribution. The fraction of the generated J/ψ decays that were fully reconstructed corresponds to the product of the acceptance and electron identification efficiency of the detector ($A \times \varepsilon_{e\mathrm{ID}}$); this is shown for electrons from decays of J/ψ at rapidity $|y| < 0.5$ in Fig. 7-a. When each simulated electron decay was weighted according to $f_{\mathrm{acc}}(\phi_{\mathrm{DCH}}, z_{\mathrm{DCH}})$ given previously, the number of reconstructed J/ψ decays was modified by 7.5%. This is essentially the variation in our acceptance calculation, using a data driven method compared to simulation. We treat this difference as a type B systematic uncertainty. The $A \times \varepsilon_{e\mathrm{ID}}$ for simulated ψ' dielectron decays in the same rapidity range was larger than that from the J/ψ by between 5-20% because of its larger mass. The maximum difference occurs at $p_T \sim$2.5 GeV/c .

The detector acceptance for charmonium also depends on the orientation of its electron decay with respect to the momentum direction of the parent particle because of the charmonium polarization. The correction factor from polarization ($\varepsilon_{\mathrm{pol}}$) was evaluated using a measurement of J/ψ polarization [18] in p+p collisions interpolated to the relevant transverse momentum. The uncertainty in $\varepsilon_{\mathrm{pol}}$ due to the uncertainty in the polarization was assigned as a type B systematic uncertainty. In the p_T region where there is no polarization measurement ($p_T > 5$ GeV/c for J/ψ and all p_T for ψ') the one standard deviation uncertainty was calculated assuming the J/ψ polarization in this region could be anything between -1 and 1. Figure 7-b shows the p_T dependence of $\varepsilon_{\mathrm{pol}}$.

The trigger (ERT) performance was studied using single electrons. We used a MB data sample to measure the p_T dependent fraction of electron candidates that fired the ERT in each of the EMCal sectors. These fractions were then used in simulation to estimate the J/ψ efficiency of the ERT trigger ($\varepsilon_{\mathrm{ERT}}$). This process was repeated for each change in the ERT operational conditions, such as a change in the energy threshold, or a significant modification in the number of EMCal or RICH sectors included in the ERT trigger. Figure 7-c shows the p_T dependence of $\varepsilon_{\mathrm{ERT}}$, weighted by the luminosity accumulated in each ERT period. When the single electron ERT efficiency of each EMCal sector was varied within its statistical uncertainty, a one standard deviation change of 4.5% in $\varepsilon_{\mathrm{ERT}}$ was observed. This deviation is shown in Fig. 7-c as the shaded band and is assigned as a type B systematic uncertainty for the J/ψ and ψ' yields. No significant change in $\varepsilon_{\mathrm{ERT}}$ was observed using the ψ' in the simulations.

The data points in the p_T dependent cross section are placed in the center of each p_T bin. Hence, a correction (bin_{shift}) was made in the cross section to account for the dominance of the yield in the lower end of each p_T bin (Fig. 7-d). In addition, the finite momentum resolution smears the measured p_T distribution. A final correction bin_{smear} is applied (Fig. 7-e) since some J/ψ decays are not reconstructed in the same p_T bin as the original which can distort how the original distribution is measured. This distortion is not accounted for in the acceptance and efficiency Monte-Carlo calculations and is estimated by smearing the p_T distributions according to expected detector momentum resolution. Type B uncertainties on the line shape of the true J/ψ p_T distribution propagates to the smearing effect as an uncertainty of 1.5%.

D. Cross section results

The J/ψ and ψ' dilepton differential cross section for each p_T bin is calculated by

$$\frac{B_{ll}^{\psi}}{2\pi p_T}\frac{d^2\sigma_{\psi}}{dydp_T} = B_{ll}^{\psi}\frac{1}{2\pi p_T}\frac{1}{\varepsilon_{\mathrm{inel}}\int \mathcal{L}dt}\frac{N_{\psi}}{\Delta y \Delta p_T A \varepsilon}, \tag{7}$$

where B_{ll}^{ψ} is the branching ratio of the charmonium states into dileptons and $\varepsilon = \varepsilon_{e\mathrm{ID}}\varepsilon_{\mathrm{ERT}}\varepsilon_{\mathrm{pol}}\varepsilon_{\mathrm{mass}}bin_{\mathrm{shift}}bin_{\mathrm{smear}}$.

All systematic uncertainties described in the previous sections are listed and classified in Table III. The quadratic sum of the correlated systematic uncertainties (type B) is between 10% and 13% of the measured J/ψ yield and between 12% and 22% of the measured ψ' yield, depending on p_T .

The p_T dependencies of the measured J/ψ and ψ' yields are shown in Fig. 8-a and Tables IV and V. The bars correspond to the quadratic sum of all type A and statistical uncertainties. Boxes represent the quadratic sum of the type B uncertainties. There is a global uncertainty (type C) of 10% coming from the minimum-bias trigger efficiency estimate.

E. $\psi'/(J/\psi)$ yield ratio and fraction of J/ψ yield coming from ψ' decays

The decay of ψ' to J/ψ cannot be measured in the current detector configuration. However, we can calculate the fraction of J/ψ coming from ψ' decays $\left(F_{\psi'}^{J/\psi}\right)$ using the ratio between the ψ' and J/ψ cross sections and the ψ' branching ratio to J/ψ ($B_{J/\psi}^{\psi'} = (58.7 \pm 0.8)\%$ [48]).

TABLE III: List of the systematic uncertainties relative to the J/ψ and ψ' dielectron yields. Ranges indicate p_T dependence.

description	contribution	type
fraction of J/ψ in the mass cut	0.4%	A
fraction of ψ' in the mass cut	3-13%	A
acceptance	7.5%	B
eID efficiency	1.1%	B
mass cut efficiency for J/ψ	1.0%	B
mass cut efficiency for ψ'	2.0%	B
heavy flavor MC used in fit for J/ψ	0.5-1.1%	B
heavy flavor MC used in fit for ψ'	4.8-10%	B
bin shift correction	3%	B
momentum smearing correction	1.5%	B
p_T, y and vertex input in ψ MC	2.0%	B
J/ψ polarization bias in acceptance	0-10%	B
ψ' polarization bias in acceptance	4-17%	B
ERT efficiency	4.5%	B
luminosity	10%	C

TABLE IV: J/ψ differential cross section in the midrapidity region ($|y| < 0.35$) followed by point-to-point uncorrelated (statistical and uncorrelated systematic uncertainties) and correlated systematic uncertainties. The global uncertainty is 10%.

		$\frac{1}{2\pi p_T}\frac{B_{ee}d^2\sigma_{J/\psi}}{dydp_T}[nb/(\mathrm{GeV}/c)^2]$		
p_T [GeV/c]	value	uncor.	corr.	multiplier
0-0.25	4.9	0.5	0.6	$\times 10^0$
0.25-0.5	3.9	0.3	0.5	$\times 10^0$
0.5-0.75	3.9	0.2	0.5	$\times 10^0$
0.75-1	3.5	0.2	0.4	$\times 10^0$
1-1.25	3.19	0.17	0.38	$\times 10^0$
1.25-1.5	2.21	0.14	0.27	$\times 10^0$
1.5-1.75	1.69	0.12	0.2	$\times 10^0$
1.75-2	1.42	0.1	0.17	$\times 10^0$
2-2.25	95	8	12	$\times 10^{-2}$
2.25-2.5	66	7	8	$\times 10^{-2}$
2.5-2.75	56	6	7	$\times 10^{-2}$
2.75-3	37	5	5	$\times 10^{-2}$
3-3.25	29	4	4	$\times 10^{-2}$
3.25-3.5	19.9	$^{+3.5}_{-3.6}$	2.4	$\times 10^{-2}$
3.5-3.75	13.6	2.8	1.7	$\times 10^{-2}$
3.75-4	10.6	2.5	1.3	$\times 10^{-2}$
4-4.25	6.89	$^{+2.3}_{-2.2}$	0.8	$\times 10^{-2}$
4.25-4.5	4.4	$^{+1.7}_{-1.6}$	0.5	$\times 10^{-2}$
4.5-4.75	4.7	$^{+1.5}_{-1.4}$	0.6	$\times 10^{-2}$
4.75-5	3.1	1.2	0.4	$\times 10^{-2}$
5-6	1.35	$^{+0.31}_{-0.32}$	$^{+0.17}_{-0.18}$	$\times 10^{-2}$
6-7	4.1	1.3	$^{+0.5}_{-0.6}$	$\times 10^{-3}$
7-8	1.6	0.7	0.2	$\times 10^{-3}$
8-9	0.37	$^{+0.37}_{-0.22}$	$^{+0.05}_{-0.06}$	$\times 10^{-3}$

TABLE V: ψ' differential cross section at $|y| < 0.35$ followed by point-to-point uncorrelated (statistical and uncorrelated systematic uncertainties) and correlated systematic uncertainties. The global uncertainty is 10%.

		$\frac{1}{2\pi p_T}\frac{B_{ee}d^2\sigma_{\psi'}}{dydp_T}$ [pb/(GeV/c)^2]	
p_T [GeV/c]	value	uncor.	corr.
0-1	67	20	9
1-2	40	11	$^{+7}_{-6}$
2-3	15	6	3
3-5	2.7	$^{+2.5}_{-1.5}$	0.5
5-7		<2.25 (90% CL)	
0-5	95	20	$^{+17}_{-15}$

$$F^{J/\psi}_{\psi'} = \frac{B^{\psi'}_{J/\psi}\sigma_{\psi'}}{\sigma_{J/\psi}}. \quad (8)$$

We start from the ratio between the ψ' and the J/ψ dielectron counts $R^{\psi'}_{J/\psi}$. Its joint probability distribution is calculated from the expected Poisson probability distributions (5) $P_{\psi'}(s_{\psi'})$ and $P_{J/\psi}(s_{J/\psi})$ for the dielectron counts in

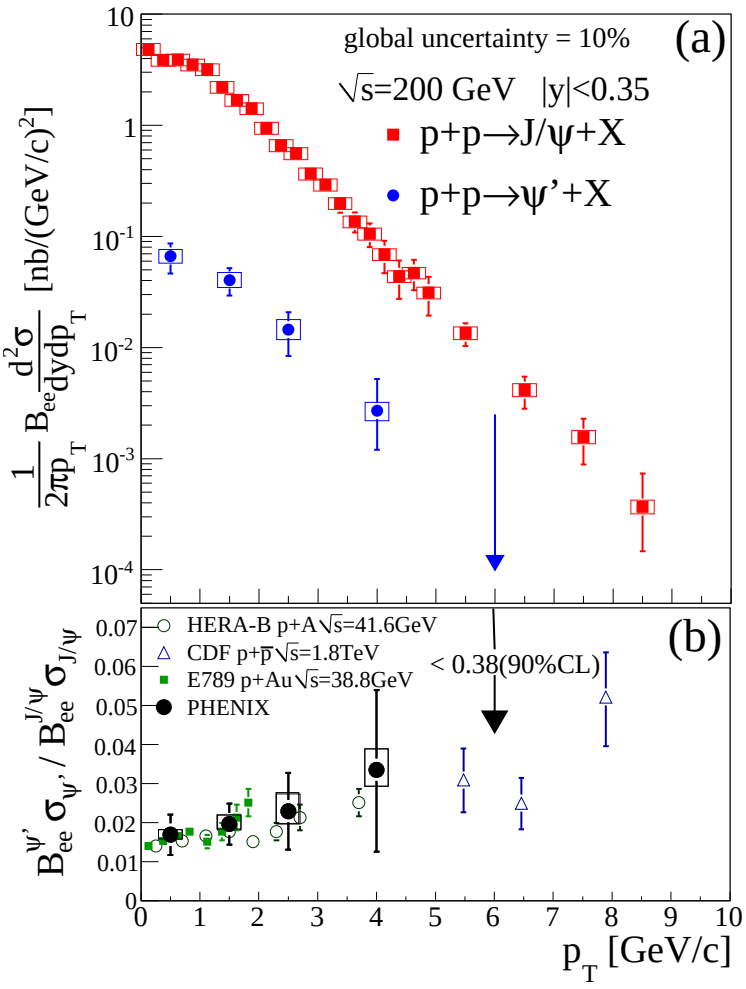

FIG. 8: (a) Transverse momentum dependence of J/ψ and ψ' yields in $|y| < 0.35$. (b) $\psi'/(J/\psi)$ ratio together with ratios obtained in other experiments. Error bars reflect statistical and type A uncertainties while boxes reflect the quadratic sum of type B uncertainties.

the ψ' and J/ψ mass ranges, respectively, and the corresponding values $f_{\psi'}$ and $f_{J/\psi}$, which account for the fraction of ψ' and J/ψ contributions in the chosen dielectron mass ranges:

$$P\left(R^{\psi'}_{J/\psi}\right) = \frac{P_{\psi'}(s_{\psi'})f_{\psi'}}{P_{J/\psi}(s_{J/\psi})f_{J/\psi}}. \tag{9}$$

The $\psi'/(J/\psi)$ dielectron cross section ratio is thus determined as follows where the different correction factors for ψ' and J/ψ must be taken into account.

$$\frac{B^{\psi'}_{e^+e^-}\sigma_{\psi'}}{B^{J/\psi}_{e^+e^-}\sigma_{J/\psi}} = \left\langle R^{\psi'}_{J/\psi}\right\rangle \frac{(A\varepsilon_{\rm eID})^{J/\psi}\varepsilon^{J/\psi}_{\rm ERT}\varepsilon^{J/\psi}_{\rm mass}\varepsilon^{J/\psi}_{\rm pol}}{(A\varepsilon_{\rm eID})^{\psi'}\varepsilon^{\psi'}_{\rm ERT}\varepsilon^{\psi'}_{\rm mass}\varepsilon^{\psi'}_{\rm pol}}. \tag{10}$$

Type A uncertainties are propagated for $f_{\psi'}$ and $f_{J/\psi}$ while common relative type B uncertainties that are correlated for J/ψ and ψ' cancel. The remaining uncertainty in the ratio comes from type B uncertainties which are not shared between the J/ψ and ψ'. The $\psi'/(J/\psi)$ dielectron cross section ratio is shown in Fig. 8-b along with results from other experiments. The numbers are listed in Table VI and a discussion of this result can be found in Sec. VI D.

Using the branching ratios, $B^{\psi'}_{e^+e^-} = 0.765 \pm 0.017\%$ and $B^{J/\psi}_{e^+e^-} = 5.94 \pm 0.06\%$ [48] in (8) gives

$$F^{J/\psi}_{\psi'} = 9.6 \pm 2.4\%. \tag{11}$$

TABLE VI: ψ' / (J/ψ) dielectron yield ratio measured at $|y|$ <0.35 followed by point-to-point uncorrelated (statistical and uncorrelated systematic uncertainties) and correlated systematic uncertainties.

		$\frac{B_{ee}^{\psi'}\sigma_{\psi'}}{B_{ee}^{J/\psi}\sigma_{J/\psi}}$ [%]	
p_T [GeV/c]	value	uncor.	corr.
0-1	1.69	0.51	$^{+0.12}_{-0.11}$
1-2	1.96	0.53	$^{+0.23}_{-0.15}$
2-3	2.3	1.0	$^{+0.5}_{-0.3}$
3-5	3.4	$^{+2.0}_{-2.1}$	$^{+0.5}_{-0.4}$
5-7		<38 (90% CL)	
0-5	2.1	0.5	

IV. RADIATIVE DECAY OF THE χ_C

The decay channel $\chi_c \to J/\psi \ +\gamma \to e^+e^- + \gamma$ is fully reconstructed in the central arms and is used to directly measure the feed-down fraction of χ_c decays in the inclusive J/ψ yield ($F_{\chi_c}^{J/\psi}$). This measurement is particularly challenging since the photon is typically of very low energy. The data sample used in this measurement and the γ identification procedure is described in Sec. IV A. The detector performance for the measurement of photon decays of the χ_c is discussed in Sec. IV B. The composition of all combinatorial and correlated backgrounds for the χ_c signal in the $e^+e^-\gamma$ mass distribution is detailed in Sec. IV C. Sec. IV D presents the final feed-down fraction calculation and a summary of all uncertainties.

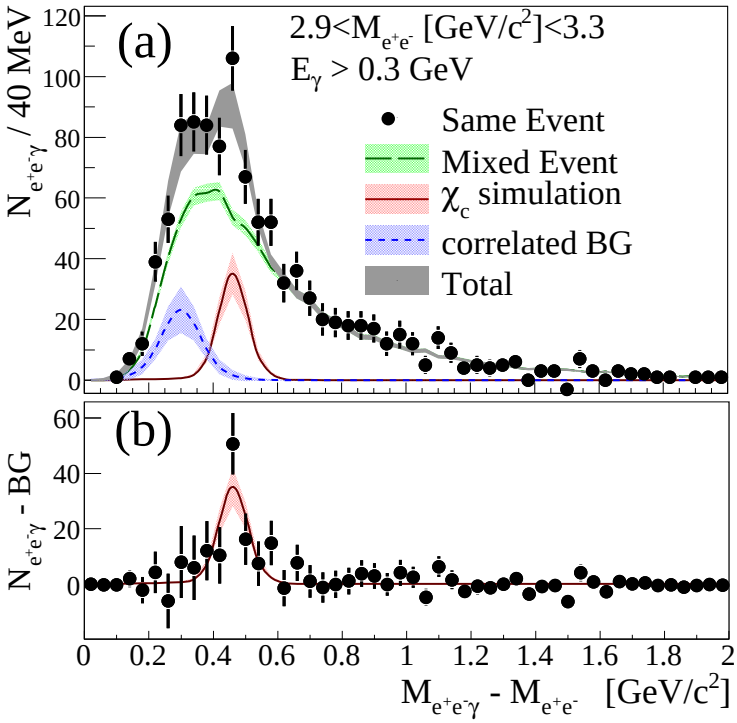

FIG. 9: (Color online) (a) $e^+e^-\gamma$ invariant mass distribution where the dielectron is required to have an invariant mass within the J/ψ mass region. The like-sign dielectron distribution is subtracted as described in the text. Bands represent the contributions from various sources: solid line - χ_c signal; long dashed line - mixed event uncorrelated background; short dashed line - Gaussian correlated background. The widths of the bands reflects the 1σ variations in the fit. (b) χ_c signal after subtraction of the backgrounds.

A. Selection of $\chi_c \to J/\psi + \gamma$ decays

The analysis of the radiative decay of the χ_c requires the identification of photons with energy (E_γ) as low as 300 MeV, the lower limit of the energy accepted in this analysis. Photons were identified as energy clusters in the EMCal whose shower shape, or profile, is consistent with an electromagnetic shower. This profile is based on the response of the EMCal to electron beam tests performed before the EMCal installation [49]. Energy clusters that were closer than four standard deviations (of the energy cluster position resolution) to reconstructed charged tracks were rejected, in order to remove electron and misidentified hadron contributions. Electrons from photon conversions in detector material which were not reconstructed by the tracking system were removed by requiring energy clusters to be further than four standard deviations from hits in the Pad Chamber, located in front of the EMCal.

The invariant mass of $e^+e^- + \gamma$ is formed using e^+e^- pairs in a tight J/ψ mass region of $2.9 < M_{e^+e^-}\,[\mathrm{GeV}/c^2] < 3.3$, avoiding the region where photons produced by bremsstrahlung can become an additional background in the 300 MeV energy region. The sample contains $N_{J/\psi}$ =2,456 $\pm$ 51 e^+e^- pairs from J/ψ decays, after removing combinatorial and correlated background as done in Sec. III A. The $e^+e^-\gamma$ mass distribution is plotted in Fig. 9-a, where we require E_γ >300 MeV. The mass of the measured e^+e^- pair is subtracted from the mass of $e^+e^-\gamma$ in order to cancel the effect of the mass resolution of the e^+e^- pair. The remaining resolution in the subtracted mass distribution is from the energy resolution of the measured photon.

B. Detector performance for the χ_c radiative decay

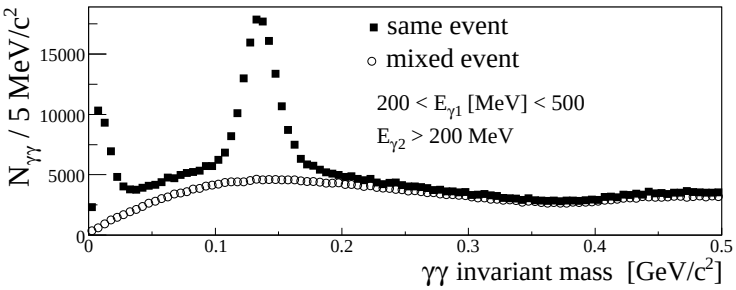

FIG. 10: $\gamma\gamma$ mass distribution in the π^0 region used to study γ detection resolution. One photon is required to have energy between 200 MeV and 500 MeV, while the other is required to have energy greater than 200 MeV.

The resolution of the mass distribution $M_{e^+e^-\gamma} - M_{e^+e^-}$ is dominated by the photon energy resolution of the EMCal. The analysis is complicated by the fact that most photons from χ_c decays have energy close to the lower limit of the EMCal sensitivity. Consequently, the behavior of the calorimeter was studied by using a sample of $\pi^0 \to \gamma\gamma$ decays in real data and in the simulations. The invariant mass of EMCal energy cluster pairs is produced in Fig. 10. No γ selection criteria is applied. After subtracting the 2γ combinatorial background determined from mixed events, the π^0 yield is obtained by fitting a Gaussian to the peak in the invariant mass distribution.

The single γ efficiency corresponds to the fraction of π^0 counts which survive the identification criteria applied to one of the photons. Figure 11-a shows the energy dependence of the photon identification efficiency ($\varepsilon_{\gamma ID}$) in real and simulated data. The simulation yields an efficiency 2.3% larger than that found in real data. This difference was included as a type B systematic uncertainty in $\varepsilon_{\gamma ID}$.

The central value of the π^0 mass peak decreases slightly as the photon energy approaches the lower limit of the calorimeter sensitivity. This behavior is caused by zero suppression during data acquisition and the energy cluster recognition algorithm. These effects are correctly reproduced in simulation as can be seen in Fig. 11-b. The γ energy resolution ($\delta E_\gamma / E_\gamma$) was uniformly degraded by 4.7% in the simulation in order to match the mass resolution ($\delta M/M$) of the π^0 peaks observed in real data (Fig. 11-c).

χ_{c1} and χ_{c2} states were generated using gluon+gluon scattering in PYTHIA with the CTEQ6M PDF, requiring that the J/ψ be in the rapidity range $|y| < 0.5$. The χ_{c0} is not considered in the simulation because of its small branching ratio to J/ψ of 1.14 ± 0.08 % [48]. Figure 12 shows the mass and γ energy distribution of $e^+e^-\gamma$ decays of simulated χ_c. The conditional acceptance of the γ from the χ_c is plotted as a function of the J/ψ momentum in Fig. 13. The geometric acceptance of the χ_c can be affected by its polarization and the polarization of the decay J/ψ. There is no measurement of the χ_c polarization, but simulation studies show that the overall acceptance is modified by at most 5.6% if the χ_c is totally transversely polarized. This possible modification was included in the acceptance type B

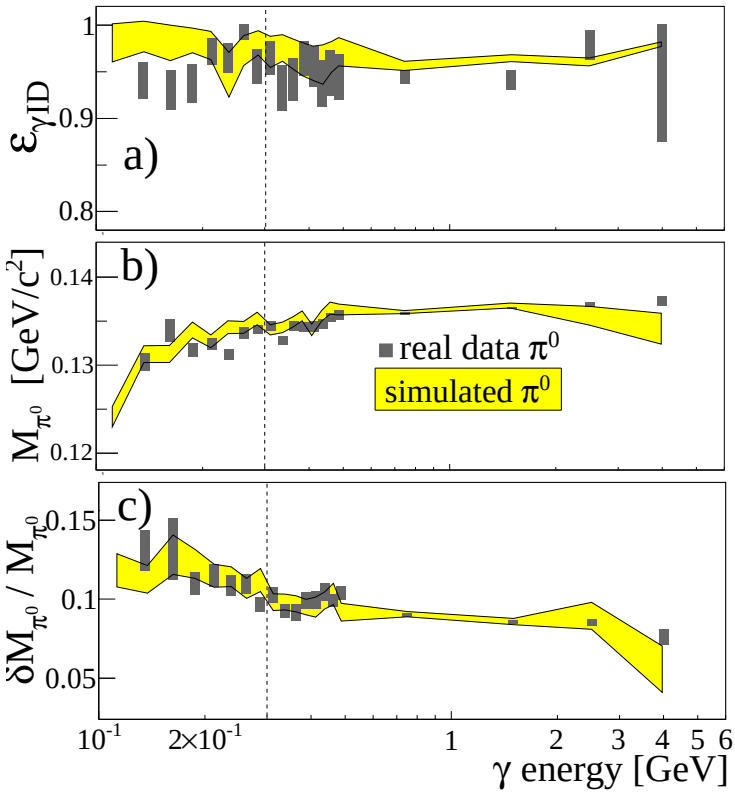

FIG. 11: (Color online) Study of the π^0 detection performance using both the measured γ energy in real data (boxes) and detector MC (shaded band). (a) γ identification efficiency, (b) π^0 mass peak position, (c) π^0 mass resolution. The vertical dashed line represents the minimum γ energy required in the χ_c analysis. Uncertainties are from the π^0 fit parameters in simulated and real data.

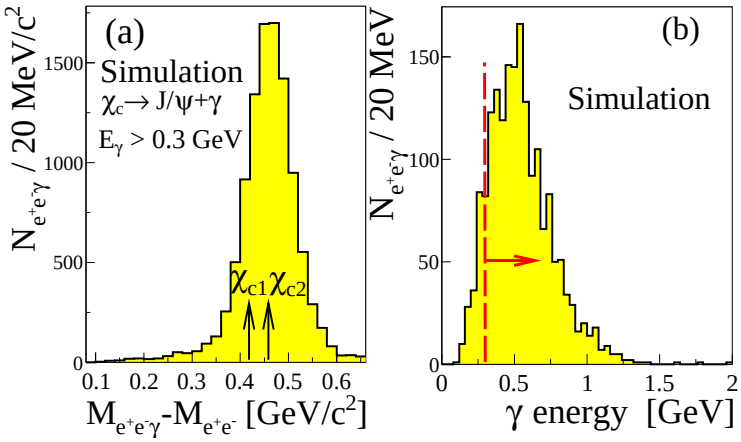

FIG. 12: (Color online) Mass (a) and γ energy (b) distributions of $e^+e^-\gamma$ decays from χ_{c1} and χ_{c2} decays obtained from PYTHIA + detector simulation. The dashed line in (b) represents the γ energy cut applied in this analysis.

systematic uncertainty.

C. Composition of the $e^+e^- + \gamma$ sample

In addition to the χ_c signal, the observed $e^+e^- + \gamma$ sample contains combinatorial background, mostly coming from uncorrelated π^0 decays present in events where a J/ψ is detected. There is also a contribution from photonic sources

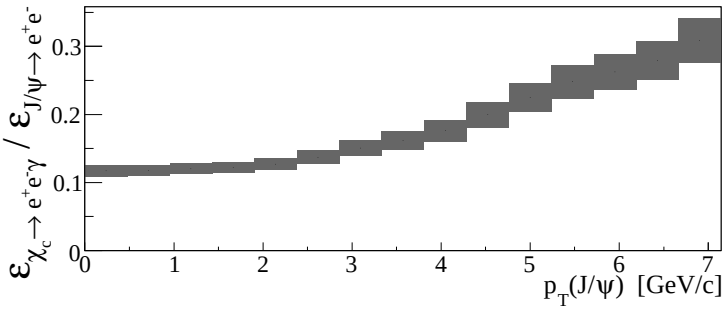

FIG. 13: Conditional acceptance and efficiency of the χ_c decay to $e^+e^-\gamma$ as a function of the J/ψ transverse momentum. The height of the boxes corresponds to the type B systematic uncertainty due to the lack of knowledge of the polarization and the photon identification efficiency.

correlated to the J/ψ , which will be discussed later.

The combinatorial background from random e^+e^- pairs (i.e. the combinatorial background to the J/ψ in the χ_c decay) is well described by the sum of $e^+e^+\gamma$ and $e^-e^-\gamma$ mass distributions. The mass distribution of random $(e^+e^-)+\gamma$ combinations (i.e. random J/ψ+γ pairs) was obtained using the invariant mass distribution of e^+e^- pairs from one event and photons from another event. In order to obtain the combinatorial background as realistically as possible, events used to form the e^+e^- and γ combination were required to have event vertices within 3 cm (2σ of the vertex position resolution) of each other.

Sources of correlated background include radiative decays of J/ψ ($J/\psi \to e^+e^-\gamma$), electron bremsstrahlung, π^0s produced in jets containing J/ψ, $\psi' \to J/\psi$+ neutral mesons, and $B^0 \to J/\psi$+ X where X or its decays includes a γ. Another possibility is that a J/ψ could be produced together with a high energy photon [50]. Recent studies also suggest an important contribution from $gg \to J/\psi + \gamma + gg$ in NNLO calculations at $\sqrt{s}$ =14 TeV [16]. No estimate was made for $\sqrt{s} = 200$ GeV at the time of this writing. These sources are considered below.

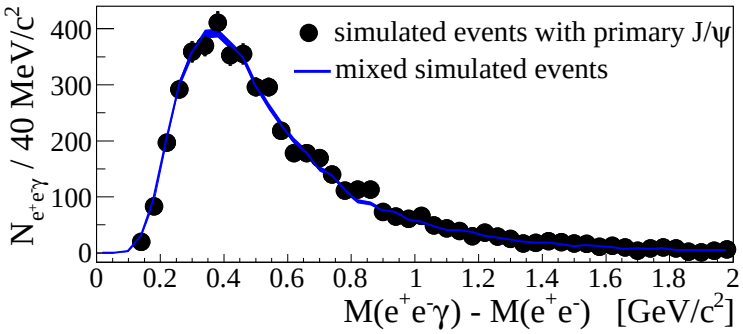

FIG. 14: (Color online) Simulated $e^+e^- + \gamma$ invariant mass distribution from PYTHIA events containing primary J/ψ decays. The line is the combinatorial background obtained using simulated mixed events from the same sample.

1. *Correlated $e^+e^-\gamma$ background from radiation and jets*

Collisions containing primary J/ψ mesons produced by gluon+gluon scattering (the dominant source) were simulated using PYTHIA in order to understand the electron radiation and jet contributions. Only the e^+e^- and the radiative $e^+e^-\gamma$ decay channels were simulated. All final state particles with momentum larger than 100 MeV and $|\eta| < 0.5$ were reconstructed, with J/ψ and γ identification criteria identical to those used in analysis of real data. The $e^+e^-\gamma$ distribution obtained from this simulation is completely accounted for by combinatorial background extracted using mixed events (Fig. 14), leaving little room for contributions from possible jets containing J/ψ, radiative decays or electron radiation when crossing the detector support. This result is not surprising since photons produced by bremsstrahlung in the detector structure are very close to their associated electron and are rejected by the criteria that remove electrons in the γ identification. The minimum dielectron mass cut of 2.9 GeV/c^2 also removes radiative J/ψ decays with $E_\gamma > 200$ MeV, i.e. those in the energy range of the photons used in this analysis.

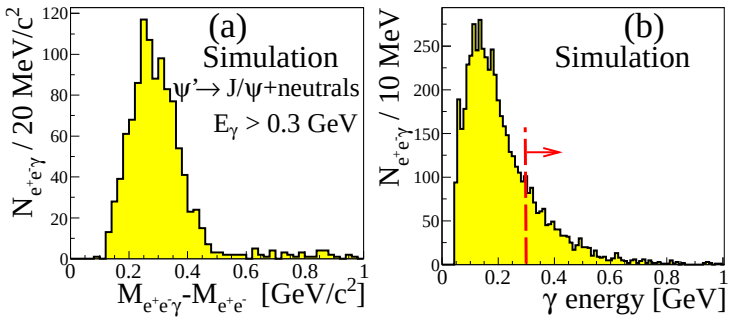

FIG. 15: (Color online) Mass (a) and γ energy (b) distributions of $\psi' \to J/\psi$+neutrals $\to e^+e^-\gamma$ obtained from simulations. Dashed lines in panel (b) represents the photon energy cut applied in this analysis. Appropriate scaling indicates that such events contribute between 6 and 20 counts to the correlated $e^+e^-\gamma$ distribution.

2. ψ' decays

In Sec. III E we reported that 9.6 ± 2.4 % of the J/ψ counts in our sample come from ψ' decays. 41.4 ± 0.9 % of these decays contain a neutral meson that decays into photons [48], namely $\psi' \to J/\psi + \pi^0\pi^0$, $\psi' \to J/\psi + \pi^0$ and $\psi' \to J/\psi + \eta$. We will refer to these decay channels collectively as $\psi' \to J/\psi + n\gamma$. Simulations show that most of the decays into neutral mesons are either not detected in the central arm acceptance or are rejected by the γ energy cut, leaving an estimated 6-20 counts in the low mass distribution of $e^+e^-\gamma$ (Fig. 15). Contributions from $\psi' \to \gamma + \chi_c \to 2\gamma + J/\psi$ decays are expected to be no larger than three counts.

3. B-meson decays

The contribution from B decays was calculated using the bottom cross section measured by PHENIX [40]. The contribution of B decays to J/ψ plus any photon is less than 3 counts in the entire $e^+e^-\gamma$ sample.

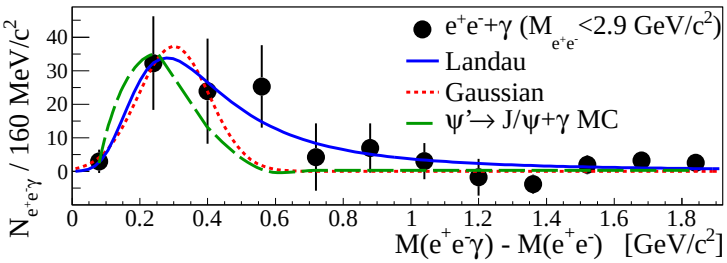

FIG. 16: (Color online) The $e^+e^-\gamma$ mass distribution in the data, after combinatorial background subtraction, where $M_{e^+e^-}$[GeV/c^2] <2.9. The lines are empirical fits as explained in the text. Note that the simulated $\psi' \to J/\psi + \gamma$ shape is arbitrarily normalized.

4. Other sources

Using real data, a check was done for possible correlated radiation backgrounds that might have been missing in the simulation. The invariant $e^+e^-\gamma$ mass distribution was formed in which we required $M_{e^+e^-}$ <2.9 GeV/c^2. The χ_c contribution is small in this region and the correlated signal should be mainly from other sources. The data, unlike the simulation, show a correlated background after combinatorial background subtraction (Fig. 16). The line shape of this mass distribution can be described by a Gaussian distribution, Landau distribution, or a simulated $\psi' \to J/\psi + \gamma$ shape. Its source could be the $gg \to J/\psi + \gamma + gg$ process mentioned previously but this is unknown. We assume the functional shape of this source is the same in the $M_{e^+e^-}$ of interest and include it in the fit to the spectrum, as described in Appendix B.

The like-sign $ee\gamma$ distribution, normalized according to Eq. (1), was subtracted from the unlike-sign distribution to give the data points in Fig. 9-a. The normalization of the combinatorial background in $e^+e^-\gamma$ using mixed events cannot be determined analytically because of small differences in the trigger efficiency in different events. The combinatorial background, different assumptions of the correlated background and the χ_c simulated mass distributions were fit to the measured distribution. Details of this fit can be found in Appendix B and the result can be seen in Fig. 9.

The fits gave 96 ± 24 counts for the χ_c . Small differences resulting from different assumptions for the correlated background (4.6%) are included as a type B systematic uncertainty. The χ_c count has a significance of four standard deviations and the signal/(combinatorial plus correlated background) was 1/5.

D. Feed-down fraction result

The fraction of J/ψ counts coming from χ_c decays is

$$F_{\chi_c}^{J/\psi} = \frac{N_{\chi_c}}{N_{J/\psi}} \frac{1}{\left\langle \varepsilon_{\chi_c}/\varepsilon_{J/\psi} \right\rangle}. \tag{12}$$

To find the mean conditional acceptance, $\left\langle \varepsilon_{\chi_c}/\varepsilon_{J/\psi} \right\rangle$, the conditional acceptance shown in Fig. 13 must be convoluted with the χ_c p_T distribution. An estimate of the χ_c p_T distribution was obtained by fitting the χ_c signal and backgrounds to a two dimensional $e^+e^-\gamma$ mass vs. p_T distribution obtained from data. While the statistical uncertainties in the resulting p_T dependent number of χ_c decays are large, the dependence of the acceptance on the p_T of the χ_c is mild, hence the uncertainty in the mean conditional acceptance is small. We obtain $(\varepsilon_{\chi_c}/\varepsilon_{J/\psi}) = \ 12.0 \pm 0.4$ %.

TABLE VII: Summary of the type B systematic uncertainties in the χ_c feed-down fraction measurement. The total gives the sum of all errors in quadrature.

syst uncertainty	contribution	type
γ ID	0.7%	B
energy resolution	1.6%	B
χ_c polarization	1.8%	B
correlated background line shape	1.5%	B
J/ψ continuum	0.1%	B
fit procedure	1.7%	B
χ_c momentum dependence	1.1%	B
TOTAL	3.6 %	

Tests of the fitting procedure and the conditional acceptance calculation were performed using different simulated data sets with varying feed-down fraction from χ_c and ψ', namely: 30%χ_c+10%ψ'+60%J/ψ, 100%χ_c, no χ_c. The feed-down observed after reproducing the analysis performed in real data on these sets of simulated events correctly returned the fraction of χ_c events with no significant bias. Variations in the minimum E_γ criteria changed the measured feed-down in the simulation by 1.7%. This variation is taken into account in the uncertainties as a type B error introduced by the analysis procedure. When the photon energy resolution is changed in the detector Monte-Carlo calculations in a manner still consistent with the measured $\pi^0 \to \gamma\gamma$ mass resolution, both the conditional acceptance and the χ_c counts returned from various fits lead to a variation of the feed-down fraction by 1.6%. The list of all systematic uncertainties is shown in Table VII.

The final χ_c feed-down fraction using (12) is

$$F_{\chi_c}^{J/\psi} = 32 \pm 9\% \tag{13}$$

when taking the quadratic sum of the statistical and systematic uncertainties.

V. J/ψ ANALYSIS IN THE FORWARD RAPIDITY REGION

This section describes the analysis performed to obtain the inclusive J/ψ dimuon yield at forward rapidity ($1.2 < |y| < 2.2$). Sec. V A describes the J/ψ signal extraction from the dimuon spectrum and related uncertainties. The response of the muon arm spectrometers to dimuon decays from the J/ψ is described in Sec. V B. Finally, the p_T and

rapidity dependence of the J/ψ differential cross section and a summary of systematic uncertainties is reported in Sec. V C.

A. $J/\psi \to \mu^+\mu^-$ signal extraction

The dimuon invariant mass spectrum was obtained from the muon sample selected according to the criteria described in Sec. II. The decomposition of the dimuon background is very similar to that described in Sec. III A for dielectrons. The combinatorial background was estimated using the mass spectrum of random pairs formed by pairing opposite-sign muon candidates from different events. The muons of the mixed pair are required to arise from collision vertices that differ by no more than 3 cm in the beam direction. The mixed event spectrum was normalized by the factor

$$\alpha = \frac{\sqrt{(N^{\rm same}_{\mu^+\mu^+})(N^{\rm same}_{\mu^-\mu^-})}}{\sqrt{(N^{\rm mixed}_{\mu^+\mu^+})(N^{\rm mixed}_{\mu^-\mu^-})}}, \tag{14}$$

where $N^{\rm same}_{\mu\mu}$ and $N^{\rm mixed}_{\mu\mu}$ are the number of pairs formed from two muons in the same or in mixed events, respectively. The mass spectrum of the dimuons in the J/ψ mass region is shown in Fig. 17.

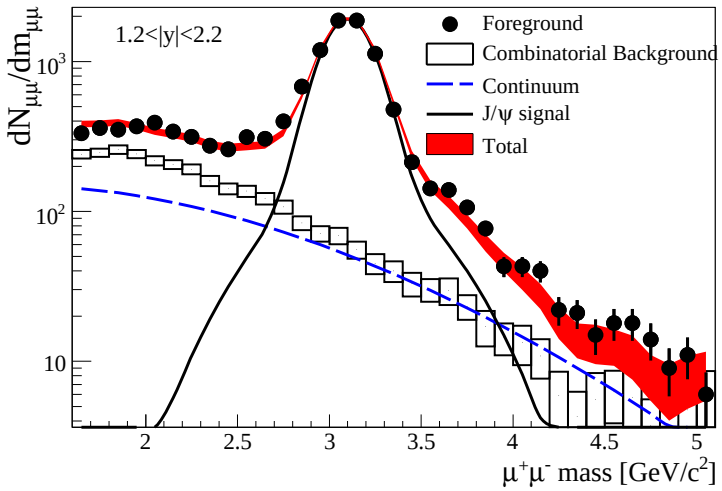

FIG. 17: (Color online) Invariant mass distribution of dimuons in the J/ψ mass region. The components of the spectrum are the combinatorial background estimated from a mixed-event technique, an acceptance-modified double Gaussian representing the J/ψ signal, and an acceptance-modified exponential continuum (see Appendix C for details).

The components of the correlated dimuon spectrum are muons sharing the same $c\bar{c}$ or $b\bar{b}$ ancestor, dimuons from Drell-Yan pairs and the J/ψ and ψ' resonances. The mass resolution is insufficient to resolve the J/ψ and ψ' in the muon arm spectrometers. However the ψ' contribution is expected to be negligible in the peak integral compared to other uncertainties on the J/ψ yield.

A function including an exponential component and a double Gaussian component was fit to the dimuon spectrum. This function takes into account the acceptance dependence of the mass distribution and is described in more detail in Appendix C. Two methods for counting J/ψ dimuon decays were considered: 1) using the fitted J/ψ component, or 2) direct counting of dimuon pairs in the mass region $2.6 < M_{\mu^+\mu^-}[{\rm GeV}/c^2] < 3.6$ with subtraction of the combinatorial background and fitted exponential continuum underneath the peak in that same region. The standard deviations of the central values of the fits and of the signal extraction method variations described in Appendix C are taken as type A signal extraction systematic uncertainties, since these variations are largely driven by statistical variations. The J/ψ count for each data set and p_T bin are listed in Appendix C. The total number of J/ψ counts was $16,612 \pm 147({\rm stat}) \pm 112({\rm syst})$ in the south muon arm and $16,669 \pm 145({\rm stat}) \pm 115({\rm syst})$ in the north muon arm.

B. Dimuon acceptance and efficiency studies

The response of the muon arm spectrometers to dimuons from J/ψ decays was studied using a GEANT3-based simulation of the muon arms and an offline MuID trigger emulator. The MuID panel-by-panel efficiency used in these

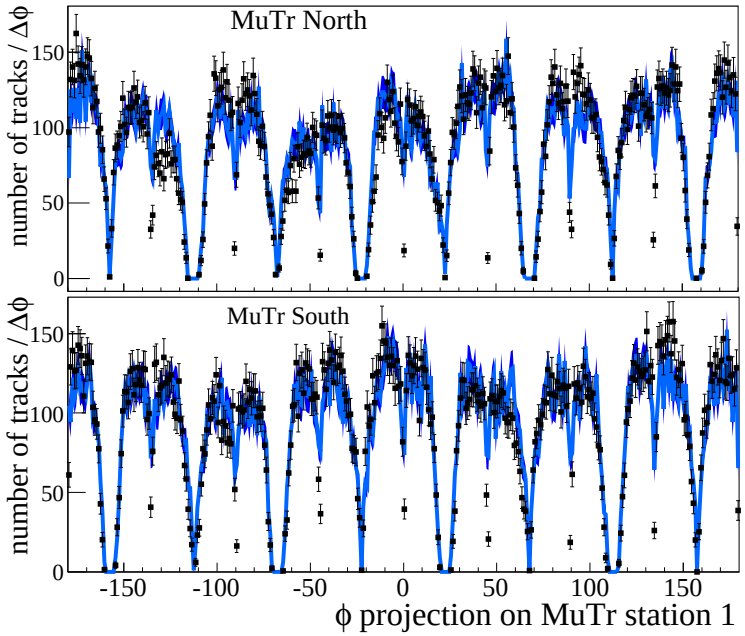

FIG. 18: (Color online) Simulated (shaded area) and real data (bars) single muons distributed in the ϕ coordinate of the MuTr.

simulations was estimated from reconstructed roads in real data, or in cases with low statistics, from a calculation based on the operational history record for each channel. A systematic uncertainty of 4% on the J/ψ yield was assigned due to the variation of the MuID efficiency during each data-taking period.

The charge distribution in each part of the MuTr observed in real data and the dead channels and their variation with time over the data-taking period were used to give an accurate description of the MuTr performance within the detector simulation. The azimuthal distribution of muon candidates in real data and simulated muons from J/ψ decays using the PYTHIA simulation are shown in Fig. 18. The z vertex distribution of simulated J/ψ decays is the same as that observed in real data, and the p_T distribution in the MuTr obtained in simulation was weighted to match that observed in real data. The relatively small differences in the real and simulated ϕ distributions visible in Fig. 18 are thought to be due primarily to missing records for short periods of time in the dead HV channel maps. These differences are estimated to change the J/ψ dimuon yields by up to 6.4 (4.0)% in north (south) arms. Run-by-run variations of the MuTr single muon yields are estimated to affect the final J/ψ yields by an additional 2%.

The J/ψ acceptance $\times$ efficiency ($A\varepsilon$) evaluation used a PYTHIA simulation with several parton distributions as input to account for the unknown true rapidity dependence of the J/ψ yield, leading to variations of 4% in the final acceptance. Figure 19 shows the overall p_T dependence of $A\varepsilon$ for J/ψ dimuon decays. The uncertainties related to the knowledge of the detector performance are point-to-point correlated (type B) between different p_T and different rapidity bins.

The uncertainty in the dimuon acceptance caused by lack of knowledge of the J/ψ polarization was studied using the detector simulation. The first preliminary results in PHENIX at forward rapidity indicate that the J/ψ polarization is no larger than ± 0.5 for $p_T < 5$ GeV/c (in the helicity frame). For this polarization variation, the simulations show one standard deviation variations between 2% and 11%, with the largest variation occurring for $p_T < 1$ GeV/c and $y \simeq 1.2$. For $p_T > 5$ GeV/c, where there are no polarization measurements we consider polarizations anywhere between ± 1, and find variations no larger than 5%. These deviations are considered as type B uncertainties.

C. J/ψ dimuon cross section result

The differential cross section for each p_T bin was calculated according to Eq. (7) and was independently obtained in the north and south muon arm spectrometers and for data recorded in 2006 and 2008. The averaging of these four momentum spectra is done using a weight for each data set based on the uncertainties for each that are uncorrelated between data sets. The measurements are consistent with each other within the overall uncertainties.

Table VIII lists the systematic uncertainties involved in this calculation. By definition the statistical and type

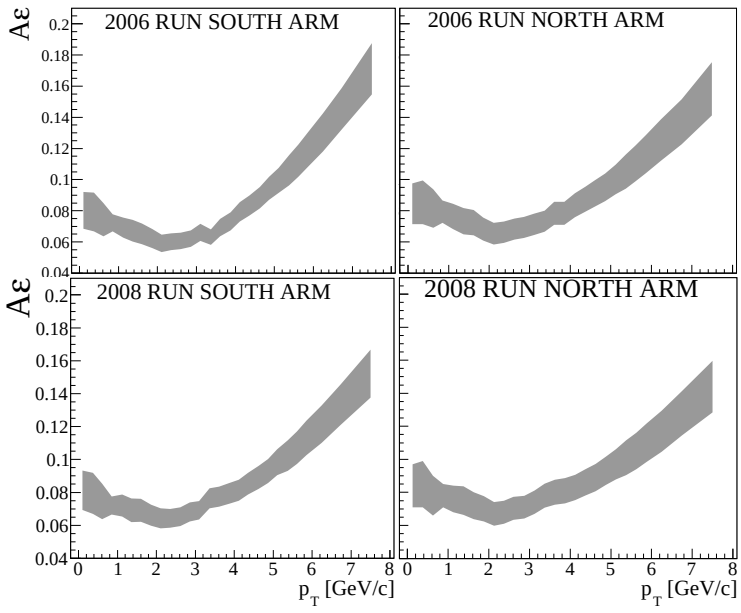

FIG. 19: Transverse momentum dependence of muon arms acceptance × efficiency for J/ψ dimuon decays in south and north muon arms during data-taking in 2006 and 2008. Shaded bands are the uncertainties of the estimates described in the text.

TABLE VIII: List of the systematic uncertainties in the J/ψ dimuon yield measurement. Ranges indicate p_T dependence.

description	relative uncertainty	type
signal extraction	1.8% - 7.7%	A
MuID efficiency	4%	B
MuTr acceptance	6.4%(north), 4.0%(south)	B
run-by-run fluctuation	2%	B
Monte Carlo J/ψ input	4%	B
J/ψ polarization	2% - 11%	B
luminosity	10%	C

A uncertainties are uncorrelated while the type C is correlated. Different type B uncertainties need to be handled differently. The uncertainties in the MuTr efficiency and run-by-run variations are also uncorrelated between data sets. The MuID efficiency and the simulation input uncertainty are correlated between different spectrometer arms and data-taking periods. Figure 20 shows the resulting average differential cross section for dimuons from J/ψ. Numerical values are listed in Table IX.

The rapidity distribution is given by:

$$B_{\mu\mu}\frac{d\sigma}{dy} = \frac{N_{J/\psi}}{\Delta y\ \varepsilon_{\rm inel}\int \mathcal{L}dtA\varepsilon}, \tag{15}$$

where the number of J/ψ counts ($N_{J/\psi}$) and the acceptance × efficiency estimates were performed for each rapidity bin.

D. p_T integrated J/ψ cross section for the central rapidity range

For the central arms, the p_T integrated J/ψ cross section was calculated using

$$B_{ee}\frac{d\sigma}{dy} = \sum_{p_T} B_{ee}\frac{d^2\sigma}{dp_T dy}\Delta p_T \tag{16}$$

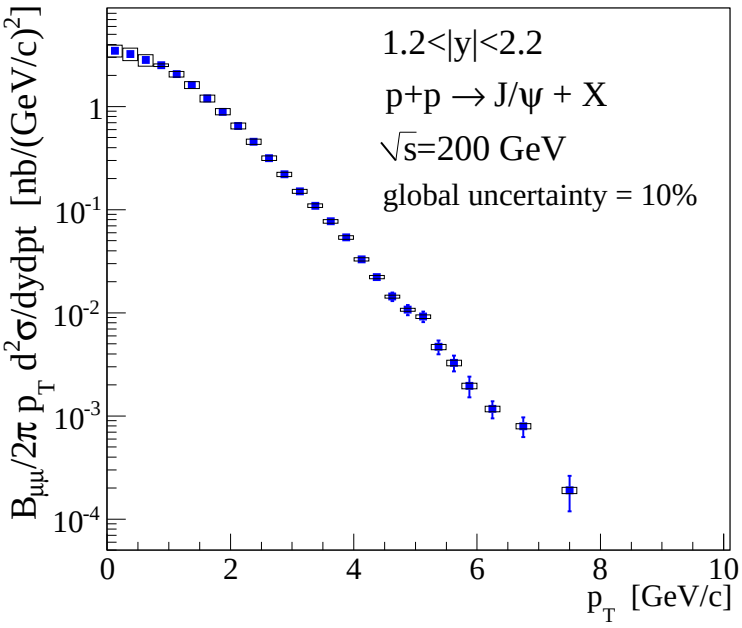

FIG. 20: Transverse momentum dependence of the J/ψ dimuon differential cross section obtained in the muon arms for data-taking in 2006 and 2008.

where $B_{ee}d^2\sigma/dp_Tdy$ is obtained from (7) using $A\varepsilon_{e\mathrm{ID}}$, $\varepsilon_{\mathrm{ERT}}$, and $\varepsilon_{\mathrm{pol}}$. The results are listed in Table X and shown in Fig. 21, where the model predictions (see discussion in Sec. VI A) are from [17, 51–53]

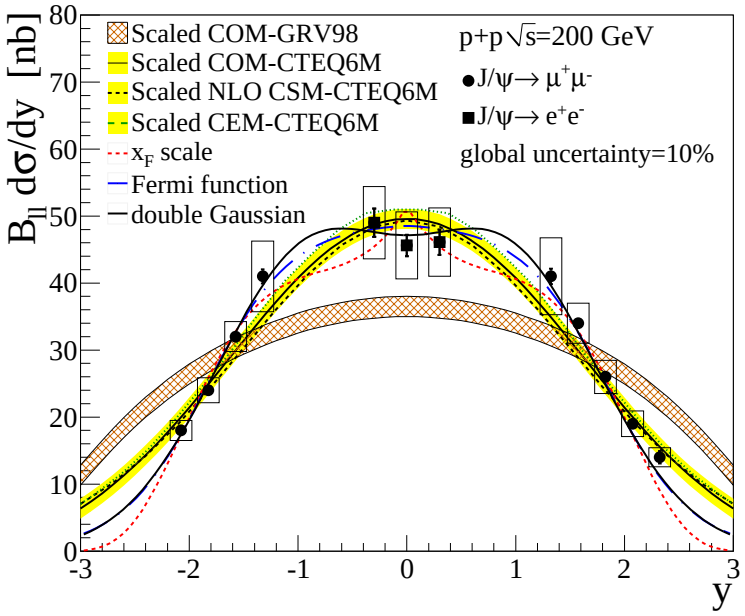

FIG. 21: (Color online) Rapidity dependence of the J/ψ yield combining dielectron (full squares) with dimuon channels (full circles) along with the fits used to estimate the total cross section. Lines correspond to the three fitting functions described in the text. Also shown are arbitrarily normalized model predictions (NRQCD [51], CEM [52, 53] and CSM [17]).

TABLE IX: Dimuon J/ψ yield in the forward rapidity region ($1.2< |y| <2.2$) followed by point-to-point uncorrelated (statistical and uncorrelated systematic uncertainties) and correlated systematic uncertainties. The global uncertainty is 10%.

		$\frac{1}{2\pi p_T}\frac{B_{\mu\mu}d^2\sigma_{J/\psi}}{dydp_T}[nb/(\mathrm{GeV}/c)^2]$		
p_T [GeV/c]	value	uncor.	corr.	multiplier
0.00-0.25	3.48	0.16	0.23	$\times 10^0$
0.25-0.50	3.24	0.10	0.22	$\times 10^0$
0.50-0.75	2.82	0.08	0.19	$\times 10^0$
0.75-1.00	2.52	0.06	0.16	$\times 10^0$
1.00-1.25	2.07	0.05	0.13	$\times 10^0$
1.25-1.50	1.62	0.04	0.10	$\times 10^0$
1.50-1.75	1.20	0.03	0.08	$\times 10^0$
1.75-2.00	8.92	0.21	0.58	$\times 10^{-1}$
2.00-2.25	6.50	0.17	0.42	$\times 10^{-1}$
2.25-2.50	4.56	0.13	0.30	$\times 10^{-1}$
2.50-2.75	3.16	0.10	0.21	$\times 10^{-1}$
2.75-3.00	2.20	0.08	0.14	$\times 10^{-1}$
3.00-3.25	1.51	0.06	0.10	$\times 10^{-1}$
3.25-3.50	1.09	0.05	0.07	$\times 10^{-1}$
3.50-3.75	7.71	0.38	0.50	$\times 10^{-2}$
3.75-4.00	5.38	0.31	0.35	$\times 10^{-2}$
4.00-4.25	3.30	0.23	0.22	$\times 10^{-2}$
4.25-4.50	2.23	0.18	0.15	$\times 10^{-2}$
4.50-4.75	1.44	0.14	0.09	$\times 10^{-2}$
4.75-5.00	1.07	0.12	0.07	$\times 10^{-2}$
5.00-5.25	9.19	1.07	0.60	$\times 10^{-3}$
5.25-5.50	4.68	0.72	0.31	$\times 10^{-3}$
5.50-5.75	3.28	0.57	0.22	$\times 10^{-3}$
5.75-6.00	1.96	0.44	0.13	$\times 10^{-3}$
6.0-6.5	1.17	0.22	0.08	$\times 10^{-3}$
6.5-7.0	7.98	1.76	0.52	$\times 10^{-4}$
7-8	1.91	0.73	0.13	$\times 10^{-4}$

TABLE X: Rapidity dependence of J/ψ yield followed by point-to-point uncorrelated (statistical and uncorrelated systematic uncertainties) and correlated systematic uncertainties. The global uncertainty is 10%.

			$B_{ll}\frac{d\sigma_{J/\psi}}{dy}[nb]$	
rapidity	ll	value	uncor.	corr.
-2.075	$\mu\mu$	17.6	0.5	1.5
-1.825	$\mu\mu$	24.4	0.4	1.9
-1.575	$\mu\mu$	31.5	0.5	2.2
-1.325	$\mu\mu$	41.2	1.1	5.3
-0.3	ee	49.0	2.1	5.4
0.0	ee	45.6	1.6	5.0
0.3	ee	46.1	1.9	5.1
1.325	$\mu\mu$	40.7	1.2	5.7
1.575	$\mu\mu$	33.6	0.7	3.0
1.825	$\mu\mu$	25.6	0.4	2.5
2.075	$\mu\mu$	18.9	0.4	1.9
2.325	$\mu\mu$	13.9	0.9	1.4

VI. RESULTS DISCUSSION

This section presents a summary of the results reported in the previous sections and compares them with results obtained in other experiments as well as predictions from several different production mechanism calculations. The rapidity dependence of the J/ψ yield is compared to models using various PDFs in Sec. VI A. The total J/ψ cross section is derived from the rapidity distribution and discussed in Sec. VI B. The J/ψ differential cross section dependence on p_T is compared to empirical scaling laws observed at lower energies as well as different charmonium hadronization

models in Sec. VI C. The measured fraction of the J/ψ yield coming from ψ' and χ_c decays is compared to other experiments in Sec. VI D. The consequences for the results presented in this article on recent charmonium measurements in $p(d)$+A and A+A collisions are discussed in Sec. VI E.

The models used in our comparisons were described in Sec. I; namely, the Color Evaporation Model (CEM), the Color Singlet Model (CSM) and nonrelativistic QCD (NRQCD). The CEM used FONLL calculations for the charm cross section and CTEQ6M for the parton distribution functions [52, 53]. For the CSM comparison, we used the recent NLO calculation only for the direct J/ψ yield at RHIC energy and PHENIX rapidity coverage [17]. We used two NRQCD calculations [20, 51] in our comparisons. The calculation performed for the direct J/ψ plus χ_c feed-down in [20] uses NLO diagrams for the color singlet and color octet states with a long range matrix element tuned from experimental hadroproduction [21] and photoproduction [22, 23] results. This calculation is only available for the differential p_T dependent cross section. An older calculation, performed for the same direct J/ψ plus χ_c feed-down with LO diagrams [51], also provides the rapidity dependence and total cross sections for different PDFs. No similar attempt has been made with the new calculations. The differential p_T dependent cross section calculation involves the emission of a hard gluon which determines the shape of the charmonium p_T spectrum. The amplitude of the hard gluon emission cannot be calculated for $p_T < 2$ GeV/c because of infrared divergences. This problem is circumvented in the older calculation by empirically constraining the low p_T nonperturbative soft gluon emission to obtain the rapidity dependence, $d\sigma/dy$. In both NRQCD calculations there is a prevalence of color octet states in the direct J/ψ contribution.

A. J/ψ rapidity dependence

The rapidity distribution of the J/ψ dilepton cross section is shown in Fig. 21 and in Table X. The data points are grouped into three rapidity ranges, corresponding to the different detectors used in the measurement: south muon arm ($-2.4 < y < -1.2$), central arms ($|y| < 0.35$) and north muon arm ($1.2 < y < 2.4$). The systematic uncertainties represented by the boxes are point-to-point correlated for data points in the same group and are uncorrelated between different groups. All points have a global uncertainty of 10% as explained in Sec. III D.

In order to compare the shape of the rapidity distribution, we normalized the CEM, CSM and NRQCD predictions to the integral of the measured data in Fig. 21. All models are available with the CTEQ6M PDFs. The NRQCD model is also available with the GRV98 [54] and the MRST99 [55] PDFs. The theoretical rapidity distributions exhibit a similar shape when using CTEQ6M. A very different rapidity distribution is obtained when the NRQCD prediction is calculated using GRV98 and MRST99 (MRST99 is not shown). These observations suggest that the choice of PDF plays the most important role in describing the shape of the J/ψ rapidity distribution. The rapidity shape also appears to be independent of the feed-down contributions, since the CSM has a similar shape to the CEM and NRQCD model, despite the fact that it contains only direct J/ψ contributions. The PDF which best describes the data is CTEQ6M and we use this for the remaining comparisons.

An empirical description of the J/ψ yield used in some fixed-target experiments with large coverage [56–63] is based on the Feynman x_F form [63],

$$\frac{d\sigma}{dx_F} = A\,(1-|x_F|)^c\,. \tag{17}$$

We can convert to a rapidity distribution by writing

$$\begin{aligned}\frac{d\sigma}{dy} &= \frac{d\sigma}{dx_F}\frac{dx_F}{dy} \\ &\approx 2A\,(1-|x_F|)^c\sqrt{\frac{\langle p_T^2\rangle + M_{J/\psi}^2}{s}}\cosh y\end{aligned} \tag{18}$$

where $\langle p_T\rangle = 1.73$ GeV/c is the average of the J/ψ p_T distributions over all measured rapidities. The fit returned $c = 16.2 \pm 0.5$ with χ^2 probability of 31%, where statistical and systematic uncertainties are summed in quadrature (Fig. 21). Figure 22 shows that c scales approximately as $c = a/\,(1 + b/\sqrt{s})$. This extrapolation of the rapidity dependence can be used to estimate the total cross section from measurements with limited rapidity coverage and will be used as one method to calculate the total cross section from the present measurement.

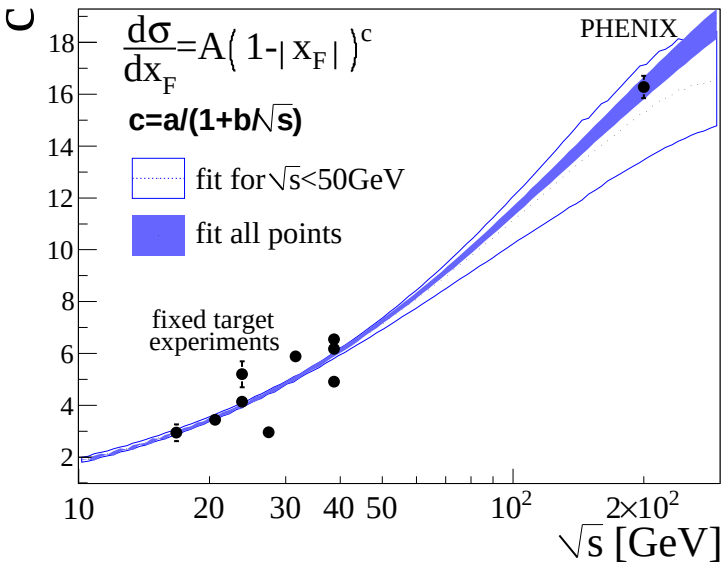

FIG. 22: (Color online) Energy dependence of the parameter c where $d\sigma/dx_F = (1-|x_F|)^c$ is fitted to x_F distributions of J/ψ production in fixed target experiments [56–63] and in the PHENIX rapidity distribution. The parameters ($a = 27.5 \pm 1.8$, $b = (141 \pm 11)$ GeV) are obtained from a fit to the experimental data points.

B. Total cross section of inclusive J/ψ

The total cross section was estimated from different empirical functions fitted to the rapidity distribution - a double Gaussian, the x_F scaling function (18) described above, and a "Fermi" function:

$$\frac{d\sigma}{dy} = \frac{A}{1+e^{\frac{(y-\lambda)}{\sigma}}} \tag{19}$$

where λ and σ are fit parameters. Rapidity distributions based on charmonium production models were not used in the total cross section in order to avoid any theoretical bias.

The correlated uncertainties between data points measured in each spectrometer were propagated to the fit uncertainty by allowing the points to move coherently in the rapidity range covered by that spectrometer. Table XI shows the total dilepton cross section and the χ^2 probability for each function used in the fit. The final cross section is obtained from the average of the numbers from each fit function. The systematic uncertainty from the unknown rapidity shape is taken from the standard deviation between the three fitting functions. Based on these fits, we conclude that the PHENIX rapidity acceptance covers 56 ± 2 % of the total J/ψ cross section. The J/ψ cross section reported in this paper is $180.1 \pm 2.0(\text{stat}) \pm 17(\text{syst})$ nb, in agreement with our previous result with a reduction in the statistical and systematic uncertainties.

TABLE XI: Estimate of the total dilepton J/ψ cross section from the three fitting functions, together with the weighted average and a comparison to the result obtained in our previous measurement. The measured total cross sections have an additional 10% global uncertainty.

estimating function	χ^2 prob.	$B_{ll}\sigma_{J/\psi}$ (nb)
x_F scale fcn, Eq. (18)	0.30	$172.2 \pm 1.6(\text{stat}) \pm 10(\text{syst})$
double Gaussian	0.96	$186.4 \pm 2.0(\text{stat}) \pm 12(\text{syst})$
Fermi fcn, Eq. (19)	0.87	$186.3 \pm 2.3(\text{stat}) \pm 12(\text{syst})$
AVERAGE		$180.1 \pm 2.0(\text{stat}) \pm 17(\text{syst})$
2005 result [10]		$178 \pm 3.0(\text{stat}) \pm 53(\text{syst})$

Table XII presents the measured total J/ψ cross section and the expectations from the three production models considered in this text. The experimental direct J/ψ cross section is estimated assuming that the feed-down fraction

of χ_c and ψ' measured at midrapidity is the same at forward rapidity. The feed-down from B mesons is only significant at high p_T and is not considered in the total cross section. The total cross section estimated using the CEM is the only one which agrees with the experimental result, although the cross section calculation includes the scale factor $\mathcal{F}$ (Sec. I) obtained from J/ψ measurements. The NRQCD includes color singlet and color octet states, and as mentioned at the beginning of this section, cannot be extrapolated to low p_T to obtain the rapidity distribution without the addition of an empirical constraint.

TABLE XII: Comparison of the measured J/ψ cross section with the three models considered in this text. Direct J/ψ cross sections are obtained assuming that the χ_c and ψ' feed-down fractions measured at midrapidity are the same at forward rapidity. Type A, type B and type C errors are quadratically summed in the measured result.

	direct J/ψ	inclusive
CEM	-	169 ± 30 nb
NLO CSM	53 ± 26 nb	-
LO NRQCD	-	140 ± 5 nb
Measured	105 ± 26 nb	181 ± 25 nb

C. J/ψ p_T distribution

Figure 23 shows the the (a) p_T and (b) $x_T = 2p_T/\sqrt{s}$ dependence of the dielectron differential cross section at midrapidity, compared to other p+p and $p + \bar{p}$ experiments [9, 21, 64–66]. The shapes of the transverse momentum distributions in Fig. 23-a follow the well known "thermal" exponential behavior for $p_T < 2$ GeV/c and a hard-scattering power law behavior at high p_T . Figure 23-b shows that the hard process scales with x_T ($\sqrt{s}^n E d^3\sigma/d^3p = G(x_T)$) [67] for x_T >0.1 in all collision energies, where $n = 5.6 \pm 0.2$ [65] (n is related to the number of partons involved in the interaction). A pure LO process leads to $n = 4$, hence, NLO terms may be important in J/ψ production [68–71].

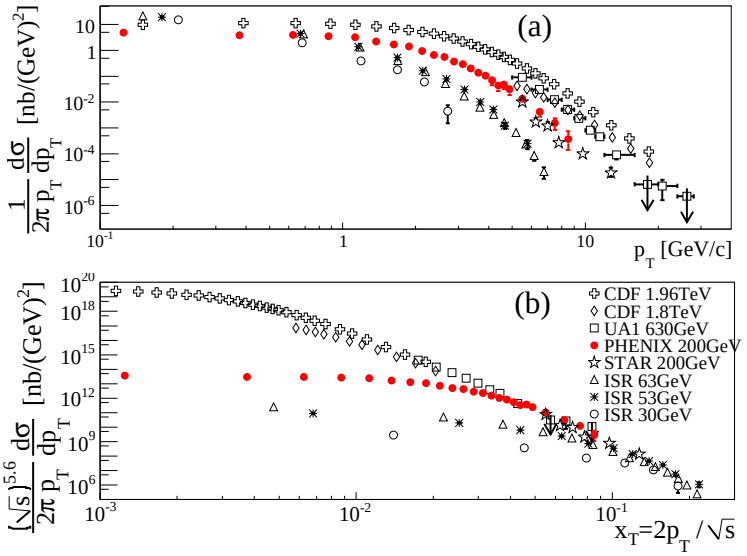

FIG. 23: (Color online) p_T distribution (a) and x_T distribution (b) of J/ψ yield in CDF [9, 21], UA1 [64], PHENIX (this work), STAR [65], and ISR [66] at $y \sim 0$.

The p_T dependence of the J/ψ differential cross sections measured at forward and midrapidity are shown in Fig. 24 along with theoretical calculations where the absolute normalization is determined in the calculations. The CEM and the NRQCD (for $p_T > 2$ GeV/c) provide reasonable descriptions of the p_T distribution, whereas the CSM disagrees in both the normalization and the slope of the p_T distribution, indicating that NLO color singlet intermediate states cannot account for the direct J/ψ production. However, the NLO CSM calculation gives a good description of the J/ψ polarization measured by PHENIX [17, 18]. Attempts are being made to extend the CSM to NNLO. Preliminary NNLO CSM calculations performed for $p_T > 5$ GeV/c [17] show a large increase in the yield, but still under- predict the experimental results. None of these theoretical models consider the B-meson decay contribution to the J/ψ yield.

The FONLL calculation [3] for these decays is also plotted in Fig. 24 and has a reasonable agreement with STAR measurements using J/ψ-hadron correlations [65]. According to this calculation, the B-meson contribution to the measured J/ψ inclusive yield is between 2%(1%) at 1 GeV/c and 20%(15%) at 7.5 GeV/c in the mid(forward)-rapidity region with large theoretical uncertainties.

The p_T spectrum of the J/ψ is harder at midrapidity, as seen from the ratio between the forward and midrapidity differential cross sections versus p_T shown in Fig. 24-bottom. Also shown are the forward/midrapidity yield ratios from the theoretical models, using their mean values and assuming that theoretical uncertainties in these ratios cancel out. All of the models predict a downward trend, but the CEM and NRQCD calculations do not follow a slope as large as the data.

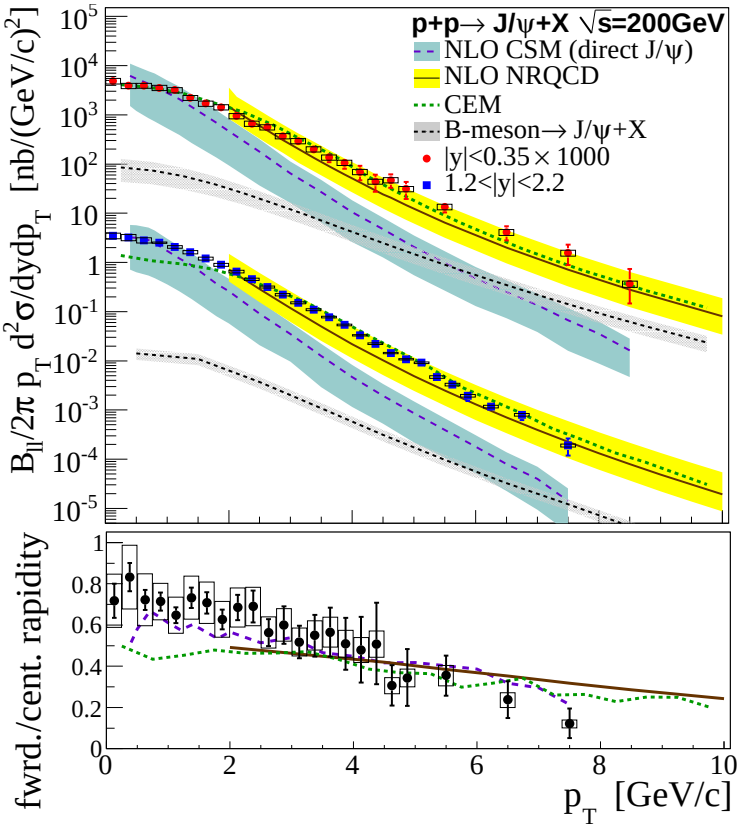

FIG. 24: (Color online) Transverse momentum dependence of (top) J/ψ yield in $|y| < 0.35$ and $1.2 < |y| < 2.2$ along with predictions based on CSM [17], NRQCD [20], CEM [52, 53] and B-meson decay based on FONLL calculation [3]. All models use CTEQ6M [44]. Boxes are systematic uncertainties. Theoretical uncertainties are represented as bands. Note that the midrapidity points are scaled up by a factor of 1000. (bottom) Ratio of the forward and central rapidity p_T spectra and corresponding theoretical predictions.

The mean transverse momentum squared, $\langle p_T^2 \rangle$, was calculated numerically from the p_T distribution. The correlated uncertainty was propagated to $\langle p_T^2 \rangle$ by moving low-p_T and high-p_T data points coherently in opposite directions according to their type B uncertainty. Table XIII shows $\langle p_T^2 \rangle$ with the propagated type A and type B uncertainties and $\langle p_T^2 \rangle$ for $p_T < 5$ GeV/c (to allow a direct comparison with the previous PHENIX results [72]). As expected, the mean transverse momentum squared is larger at midrapidity than at forward rapidity.

TABLE XIII: Mean transverse momentum squared in $(\mathrm{GeV}/c)^2$ of J/ψ and ψ' for different rapidity and p_T ranges. Uncertainties are type A and type B, respectively.

system	$\langle p_T^2 \rangle$	$\langle p_T^2 \rangle\big\|_{p_T<5\mathrm{GeV}/c}$
J/ψ $1.2 < \|y\| < 2.2$	3.63±0.03±0.09	3.43±0.02±0.08
J/ψ $\|y\| < 0.35$	4.41±0.14±0.18	3.89±0.11±0.15
ψ' $\|y\| < 0.35$	$4.7\ ^{+1.5}_{-1.05}$ ±0.4	$4.7^{+1.5}_{-1.05}$ ±0.4

D. Charmonia ratios and J/ψ feed-down fractions

The transverse momentum dependence of the $\psi'/(J/\psi)$ yield ratio (Fig. 8-b) is consistent with that observed in other experiments. Figure 25 shows the collision-energy dependence of the $\psi'/(J/\psi)$ yield ratio in low-atomic-mass fixed-target p+A, p+p , and p+$\bar{p}$ [9, 64, 66, 73–75] collisions. The ratios from $p+\bar{p}$ experiments were calculated using the reported J/ψ and ψ' cross sections for $p_T > 5$ GeV/c together with their point-to-point uncorrelated uncertainties[3]. The B meson decay contribution was removed from the J/ψ and ψ' yields, in the case of the CDF experiment [9]. Only E705 [73] has broad coverage ($-0.1 < x_F < 0.5$), while the other experiments shown have a rapidity coverage of $|y| < 0.6$. A weak trend of increasing $\psi'/(J/\psi)$ yield ratio for higher collision energy (Fig. 25) and for higher p_T (Fig. 8-b) can be observed. As mentioned earlier, the ψ' feed-down fraction of 9.7 ± 2.4 % is in agreement with the world average of 8.1 ± 0.3 % calculated in [76].

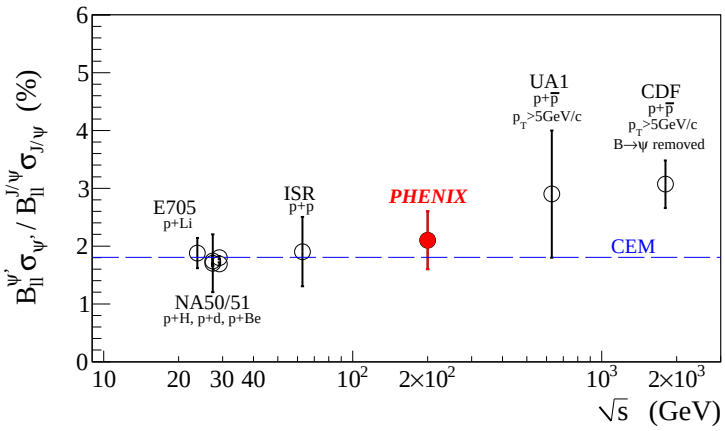

FIG. 25: (Color online) Collision-energy dependence of the $\psi'/(J/\psi)$ dilepton cross section ratio obtained in low-atomic-mass fixed-target p+A (E705 [73], NA50/51 [74, 75]) p+p (ISR [66], this result), and p+$\bar{p}$ (UA1 [64], CDF [9]) collisions. The dashed (blue) line shows the CEM calculation [52]. Statistical and systematic errors were quadratically summed.

Figure 26 compares the feed-down fraction obtained from our $\chi_c \to J/\psi + \gamma$ measurement with other experiments over a broad range of collision energy and x_F, as well as over many different colliding species [73, 77–84]. The value measured in this work, $F_{\chi_c}^{J/\psi} = 32 \pm 9\%$, is consistent with the world average of 25 ± 5 % after accounting for A dependencies in the fixed target experiments [76][4]. CEM estimate an energy and p_T independent χ_c feed-down of 40% [52] whereas recent NLO NRQCD calculations estimate 25-30% at $p_T = 10$ GeV/c [85]. Therefore, are both consistent with the data.

[3] This may be an overestimate of the systematic errors, given that a good fraction of the J/ψ and ψ' yields may be correlated.
[4] The world average was obtained after extrapolating the dependence of the estimated path length in nuclear matter for the p+A fixed target experiments.

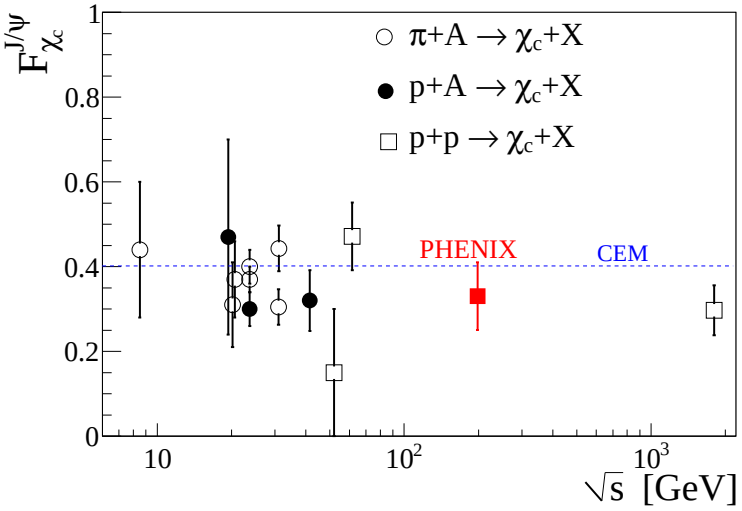

FIG. 26: (Color online) Collision energy dependence of χ_c feed-down to J/ψ measured in p+p and p+A collisions [73, 77–84] The dashed (blue) line shows the CEM calculation [52].

Combining the results of feed down from the ψ' and the χ_c we obtain a total J/ψ feed-down fraction measured in the midrapidity region of 42 ± 9 %.

E. Outcomes for heavy ion collisions

The feed-down fractions from the ψ' and χ_c have important implications for survival rates of charmonium states when either ordinary nuclear matter or high energy density nuclear matter is involved. Because of their larger size compared to the J/ψ, excited charmonium states may have a different breakup cross section in nuclear matter. This effect can modify the feed-down fractions in p+A collisions. On the other hand, if the $c\bar{c}$ is not formed as a color singlet, it can cross the nuclear matter as a colored preresonant state [86]. If this were true, the breakup cross section of J/ψ and ψ' should be the same and there would be no modification of the ψ' feed-down fraction in p+A collisions, whereas a possible modification can occur for the χ_c since it is expected to be formed mainly as a color singlet. Given the large statistical uncertainties in all measured $\psi'/$ (J/ψ) ratios shown in Figs. 8-b and 25, differences between $p+p$ and p+A are impossible to see, and therefore no conclusion about possible cold nuclear matter effects can be made at this time. The same is true for the χ_c feed-down fraction in Fig. 26. Higher precision measurements of charmonium states in p+p and d+Au collisions in the future may allow an improved determination of these possible cold nuclear matter effects on the feed-down fraction.

The behavior of charmonium states in the high density hot nuclear matter created in heavy ion collisions has long been of interest [1]. Spectral function computations [2] indicate that the χ_c and ψ' states should dissociate due to color screening at a lower temperature in hot nuclear matter than the J/ψ. One of the most important implications of the observed feed-down fractions is that the complete dissociation of the χ_c and ψ' states would lead to a 42 $\pm$ 9 % J/ψ suppression. The measured nuclear modification factor of J/ψ mesons in central Au+Au collisions at $\sqrt{S_{NN}}$ =200 GeV [28] implies a suppression of 74 $\pm$ 6 % at midrapidity and 84 $\pm$ 6 % at forward rapidity. Hence, the complete dissociation of the excited states of charmonium and the associated loss of the J/ψ yield cannot completely explain its suppression observed in Au+Au collisions. Cold nuclear matter effects and the possible dissociation of direct J/ψ by color-screening could presumably account for the remaining suppression.

VII. SUMMARY AND CONCLUSIONS

In conclusion, we have measured the yields of the three most important charmonium states in p+p collisions at $\sqrt{s} = 200$ GeV, where gluon fusion is expected to be the dominant production process. These results are the baseline for PHENIX measurements of the nuclear-modification factor, R_{AA}, in nucleus-nucleus collisions [26, 27]. The rapidity dependence of J/ψ production supports the use of CTEQ6M [44] to describe the gluon distribution in protons. The inclusive J/ψ yield is in agreement with current models which involve the initial formation of colored charmonium states, as in the CEM [52, 53] or the color octet states of the NRQCD models [51]. The inclusive J/ψ yield observed

at midrapidity comprises $9.6 \pm 2.4\%$ of ψ' decays and $32 \pm 9\%$ of χ_c decays. This result is in agreement with other experiments. Given the current large statistical uncertainties, no conclusion can be made about collision energy or p_T dependence of these fractions. The J/ψ suppression observed in Au+Au collisions cannot be totally explained by the dissociation of ψ' and χ_c, given the feed-down fraction results presented.

Acknowledgments

We thank the staff of the Collider-Accelerator and Physics Departments at Brookhaven National Laboratory and the staff of the other PHENIX participating institutions for their vital contributions. We also thank Jean Philippe Lansberg, Mathias Butenschön, and Ramona Vogt for the valuable CSM, NRQCD, CEM and FONLL calculations in the PHENIX acceptance. We acknowledge support from the Office of Nuclear Physics in the Office of Science of the Department of Energy, the National Science Foundation, a sponsored research grant from Renaissance Technologies LLC, Abilene Christian University Research Council, Research Foundation of SUNY, and Dean of the College of Arts and Sciences, Vanderbilt University (U.S.A), Ministry of Education, Culture, Sports, Science, and Technology and the Japan Society for the Promotion of Science (Japan), Conselho Nacional de Desenvolvimento Científico e Tecnológico and Fundação de Amparo à Pesquisa do Estado de São Paulo (Brazil), Natural Science Foundation of China (P. R. China), Ministry of Education, Youth and Sports (Czech Republic), Centre National de la Recherche Scientifique, Commissariat à l'Énergie Atomique, and Institut National de Physique Nucléaire et de Physique des Particules (France), Ministry of Industry, Science and Tekhnologies, Bundesministerium für Bildung und Forschung, Deutscher Akademischer Austausch Dienst, and Alexander von Humboldt Stiftung (Germany), Hungarian National Science Fund, OTKA (Hungary), Department of Atomic Energy and Department of Science and Technology (India), Israel Science Foundation (Israel), National Research Foundation and WCU program of the Ministry Education Science and Technology (Korea), Ministry of Education and Science, Russian Academy of Sciences, Federal Agency of Atomic Energy (Russia), VR and the Wallenberg Foundation (Sweden), the U.S. Civilian Research and Development Foundation for the Independent States of the Former Soviet Union, the US-Hungarian Fulbright Foundation for Educational Exchange, and the US-Israel Binational Science Foundation.

Appendix A: Fitting components of the dielectron mass distribution

The composition of the correlated dielectron mass distribution was studied by simulation of the several known sources listed in Sec. III A. Two-dimensional dielectron mass vs p_T histograms H were filled with events from the following sources:

$H_{J/\psi}(m, p_T)$ for the dielectron decay $J/\psi \to e^+e^-$

$H_{J/\psi\gamma}(m, p_T)$ for the radiative decay $J/\psi \to e^+e^-\gamma$

$H_{\psi'}(m, p_T)$ for $\psi' \to e^+e^-$

$H_{c\bar{c}}(m, p_T)$ for correlated $c\bar{c}$ pairs

$H_{b\bar{b}}(m, p_T)$ for correlated $b\bar{b}$ pairs

$H_{DY}(m, p_T)$ for Drell-Yan pairs.

The simulated two-dimensional histograms had bin widths adjusted to provide adequate statistics in each bin of the real data so that Gaussian probabilities could be assumed for each bin. The histograms were fit to the real data two-dimensional histogram in the mass range $2.0 < M_{e^+e^-}[\mathrm{GeV}/c^2] < 8.0$ according to

$$
\begin{aligned}
\frac{d^2N_{e^+e^-}}{dmdp_T} &= A_{J/\psi}H'_{J/\psi}(m,p_T) \\
&+ A_{J/\psi\gamma}H'_{J/\psi\gamma}(m,p_T) \\
&+ A_{\psi'}H'_{\psi'}(m,p_T) \\
&+ A_{c\bar{c}}H_{c\bar{c}}(m,p_T) \\
&+ A_{b\bar{b}}H_{b\bar{b}}(m,p_T) \\
&+ A_{DY}H_{DY}(m,p_T) \\
H'_{J/\psi}(m,p_T) &= \int \frac{H_{J/\psi}(m',p_T)}{\sqrt{2\pi}\sigma_{\rm ext}} e^{-\frac{(m-m')^2}{2\sigma^2_{\rm ext}}} dm' \\
H'_{J/\psi\gamma}(m,p_T) &= \int \frac{H_{J/\psi\gamma}(m',p_T)}{\sqrt{2\pi}(\sigma_{\rm ext}+\sigma_{\rm int})} e^{-\frac{(m-m'-m_{shift})^2}{2(\sigma_{\rm ext}+\sigma_{\rm int})^2}} dm' \\
H'_{\psi'}(m,p_T) &= \int \frac{H_{\psi'}(m',p_T)}{\sqrt{2\pi}\sigma_{\rm ext}} e^{-\frac{(m-m')^2}{2\sigma^2_{\rm ext}}} dm'.
\end{aligned}
\tag{A1}
$$

The expected sources are normalized in the fit by the free parameters $A_{J/\psi}$, $A_{J/\psi\gamma}$, $A_{\psi'}$, $A_{c\bar{c}}$ and $A_{b\bar{b}}$. A_{DY} was fixed according to expectations from the NLO calculations [37]. The resonance contributions $H'_{J/\psi}$, $H'_{J/\psi\gamma}$ and $H'_{\psi'}$ are smeared versions of the simulated mass spectra accounting for differences in the mass resolution between simulation and data. The free parameters controlling these smearing factors are $\sigma_{\rm ext}$ and $\sigma_{\rm int}$ which correspond to the dielectron channels and the radiative channel, respectively. The mass peak width $\sigma_{\rm int}$ and position m_{shift} parameters of the radiative J/ψ decay are determined in the fit. The fraction of radiative J/ψ decays is compared to QED calculations in Sec. III A. No mass shift parameters are needed for the J/ψ and ψ'. The fitting result is shown in Fig. 3 and its interpretation is found in Sec. III A.

Appendix B: Fitting the composition of the $e^+e^-\gamma$ mass distribution.

The composition of the $e^+e^-\gamma$ mass distribution used in χ_c analysis was studied with several simulations and mixed event mass distribution as explained in Sec. IV C. The mass distributions were:

$H_{\rm comb}(M)$ for the mass distribution using dielectrons and photons from different event to reproduce the combinatorial background

$H_{\rm cor}(M)$ for the correlated background, three assumptions were considered:

- Gaussian distribution centered at the minimum photon energy cut (300 MeV)
- Landau distribution with maximum value at the minimum photon energy
- mass distribution obtained in $\psi' \to J/\psi$ + neutral mesons simulation shown in Fig. 15-a

$H_{\chi_c}(M)$ for the mass distribution obtained in $\chi_c \to J/\psi + \gamma$ is shown in Fig. 12-a.

These mass distributions were fitted to real data using the function:

$$
\begin{aligned}
\frac{dN_{ee\gamma}}{dM} &= A_{\rm comb}H_{\rm comb}(M) + A_{\rm cor}H_{\rm cor}(M) \\
&+ A_{\chi_c}H_{\chi_c}(M) \\
H_{\rm cor}(M) &= \begin{cases} \frac{1}{\sqrt{2\pi\sigma^2}} e^{-\frac{(M-M_0)}{2\sigma^2}} & \text{(Gaussian)} \\ \frac{1}{\pi}\int_0^\infty e^{-t\log t - \frac{M-M_0}{\sigma}t}\sin(\pi t)dt & \text{(Landau)} \\ H_{\psi'}(M) & \psi' \to J/\psi + \gamma \end{cases} \\
M &= M_{e^+e^-\gamma} - M_{e^+e^-} \\
M_0 &\equiv \text{Minimum } \gamma \text{ energy} = 0.3 \text{ GeV}.
\end{aligned}
\tag{B1}
$$

The free parameters are the weighting factors $A_{\rm comb}$, $A_{\rm cor}$, A_{χ_c} and the width σ, when using Gaussian or Landau distributions as correlated background. The fit result when using a Gaussian correlated background is shown in Fig. 9

TABLE XIV: χ_c counts obtained when fitting Eq. (B1) to the $e^+e^-\gamma$ mass distribution using different assumptions for the correlated background.

correlated BG assumption	p-value of the fit	χ_c count
Gaussian	16.7%	103 ± 20
Landau	13.1%	87 ± 19
ψ' simulation	17.7%	99 ± 24

together with the fit uncertainties represented as bands. The resulting χ_c counts for each correlated background assumption are listed in Table XIV.

The average χ_c count was 96 ± 24. The standard variation of these three counts was 4.6% which is considered as a systematic uncertainty.

Appendix C: Fitting used to extract the J/ψ signal in the dimuon mass distribution.

The dimuon mass distribution can be represented by a function $F(M_{\mu\mu})$ including the combinatorial background $F_{CB}(M_{\mu\mu})$, obtained from the normalized mixed event distribution, an exponential shape accounting for the continuum distribution, a double Gaussian which describes the line shape of J/ψ in the Monte-Carlo calculation, and acceptance dependence:

$$F(M_{\mu\mu}) = F_{CB}(M_{\mu\mu}) + Acc(M_{\mu\mu})\left[F_{\psi}(M_{\mu\mu}) + A_{\rm cont}e^{-\frac{M_{\mu\mu}}{b_{\rm cont}}}\right] \tag{C1}$$

$$F_{\psi}(M_{\mu\mu}) = A_{\psi}\left[(1-f_{G2})G\left(M_{\mu\mu};M_{J/\psi},\sigma_{G1}\right) + f_{G2}G\left(M_{\mu\mu};M_{J/\psi}+\delta_M,\sigma_{G2}\right)\right] \tag{C2}$$

$$G(M_{\mu\mu};M,\sigma) = \frac{1}{\sqrt{2\pi}\sigma}e^{-\frac{(M_{\mu\mu}-M)^2}{2\sigma^2}} \tag{C3}$$

where $Acc(M_{\mu\mu})$ is the mass dependence of the dimuon acceptance estimated using simulation (Fig. 27), the J/ψ signal is fit to a double Gaussian with parameters A_ψ for the amplitude, σ_{G1} and σ_{G2} for the width of the two Gaussians, $M_{J/\psi}$ for the mean of the first Gaussian, δM for the offset of the mean of the second Gaussian, and f_{G2} for the fractional contribution of the second Gaussian. The normalization of the continuum contribution is $A_{\rm cont}$ and its exponential slope is $b_{\rm cont}^{-1}$. The predicted J/ψ counts may then be extracted as:

$$N_{J/\psi} = \int Acc(M)F_{\psi}(M)\,dM$$

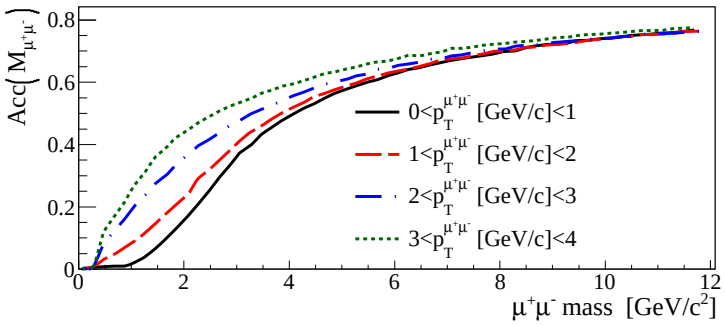

FIG. 27: (Color online) Mass dependence of the dimuon geometric acceptance in the muon arm spectrometers.

The mass distribution function $F(M_{\mu\mu})$ was fit to the measured unlike-sign dimuon mass distribution for each p_T and rapidity range using the maximum likelihood method. The mass resolution obtained in the entire J/ψ sample was $\sigma_{G1}/M_{J/\psi} = 4\%$ ($\sigma_{G1} = 125$ MeV). The fitting procedure was performed in two steps:

1. over the p_T and rapidity unbinned dimuon sample (Fig. 17) in order to determine the line shape of the J/ψ peak (σ_{G1}, σ_{G2}, δ_M and f_{G2})

2. for individual p_T and rapidity bins using fixed parameters determined in step (1).

The J/ψ mass, $M_{J/\psi}$, was allowed to vary by 10% of its nominal value (3.096 GeV/c^2) in the fitting procedure. The J/ψ and continuum amplitudes were constrained to avoid unphysical negative values. The exponential slope was allowed to vary by 20% from the value found in a fit to the entire (unbinned) sample. For the systematic uncertainty evaluation, f_{G2} was changed by ±25%, the fit was performed in two mass ranges ($1.8 < M_{\mu\mu}$[GeV/c^2] <7.0 and $2.2< M_{\mu\mu}$[GeV/c^2] <6.0) and the combinatorial background normalization α was varied by ±2%. Table XV shows the J/ψ counts obtained from the dimuon decay analysis of four different data sets, determined using the fit function (C1).

TABLE XV: J/ψ counts obtained from the dimuon decay analysis of four different data sets, determined using the fit function (C1): The "S" and "N" following 2006 and 2008 indicate the data sets for the south and north forward arms, respectively. Uncertainties are statistical only.

p_T [GeV/c]	2006 S	2006 N	2008 S	2008 N
0.00-0.25	274 ± 18	226 ± 17	182 ± 15	202 ± 17
0.25-0.50	733 ± 30	703 ± 30	459 ± 25	552 ± 27
0.50-0.75	1036 ± 37	901 ± 33	692 ± 30	684 ± 30
0.75-1.00	1155 ± 38	1048 ± 35	961 ± 34	942 ± 35
1.00-1.25	1192 ± 38	1108 ± 36	879 ± 33	946 ± 34
1.25-1.50	1102 ± 37	1043 ± 34	825 ± 31	836 ± 31
1.50-1.75	962 ± 34	876 ± 31	700 ± 28	722 ± 29
1.75-2.00	816 ± 32	641 ± 27	590 ± 26	624 ± 27
2.00-2.25	604 ± 26	572 ± 25	490 ± 24	457 ± 23
2.25-2.50	522 ± 25	437 ± 23	351 ± 21	371 ± 21
2.50-2.75	407 ± 22	335 ± 20	287 ± 18	288 ± 18
2.75-3.00	316 ± 19	263 ± 17	208 ± 16	245 ± 17
3.00-3.25	239 ± 17	230 ± 16	170 ± 15	161 ± 14
3.25-3.50	197 ± 16	180 ± 15	154 ± 13	116 ± 12
3.50-3.75	157 ± 14	125 ± 12	117 ± 12	114 ± 12
3.75-4.00	108 ± 12	103 ± 11	98 ± 11	84 ± 10
4.00-4.25	88 ± 11	71 ± 9	54 ± 8	55 ± 8
4.25-4.50	67 ± 10	53 ± 8	49 ± 8	34 ± 7
4.50-4.75	43 ± 8	34 ± 7	41 ± 7	30 ± 6
4.75-5.00	37 ± 7	26 ± 6	44 ± 10	29 ± 6
5.00-5.25	47 ± 9	28 ± 6	22 ± 6	19 ± 5
5.25-5.50	33 ± 8	15 ± 5	12 ± 4	10 ± 4
5.50-5.75	26 ± 7	12 ± 4	14 ± 5	6 ± 3
5.75-6.00	20 ± 6	12 ± 4	7 ± 4	3 ± 2
6.00-6.50	13 ± 5	10 ± 4	19 ± 5	9 ± 4
6.5-7.0	12 ± 5	8 ± 4	7 ± 3	9 ± 4
7.0-8.0	7 ± 4		5 ± 3	

[1] T. Matsui and H. Satz, Phys. Lett. B **178**, 416 (1986).
[2] A. Mócsy and P. Petreczky, Phys. Rev. Lett. **99**, 211602 (2007).
[3] M. Cacciari, P. Nason, and R. Vogt, Phys. Rev. Lett. **95**, 122001 (2005).
[4] A. Adare et al. (PHENIX Collaboration), Phys. Rev. Lett. **97**, 252002 (2006).
[5] H. Fritzsch, Phys. Lett. B **67**, 217 (1977).
[6] J. F. Amundson, O. J. P. Eboli, E. M. Gregores, and F. Halzen, Phys. Lett. B **390**, 323 (1997).
[7] R. Baier and R. Ruckl, Phys. Lett. B **102**, 364 (1981).
[8] P. L. Cho and A. K. Leibovich, Phys. Rev. D **53**, 6203 (1996).
[9] F. Abe et al. (CDF Collaboration), Phys. Rev. Lett. **79**, 572 (1997).
[10] A. Adare et al. (PHENIX Collaboration), Phys. Rev. Lett. **98**, 232002 (2007).
[11] J. M. Campbell, F. Maltoni, and F. Tramontano, Phys. Rev. Lett. **98**, 252002 (2007).
[12] P. Artoisenet, J. P. Lansberg, and F. Maltoni, Phys. Lett. B **653**, 60 (2007).
[13] B. Gong and J.-X. Wang, Phys. Rev. Lett. **100**, 232001 (2008).
[14] P. Artoisenet, J. M. Campbell, J. P. Lansberg, F. Maltoni, and F. Tramontano, Phys. Rev. Lett. **101**, 152001 (2008).
[15] J. P. Lansberg, Eur. Phys. J. C **61**, 693 (2009).
[16] J. P. Lansberg, Phys. Lett. B **679**, 340 (2009).
[17] J. P. Lansberg, Phys. Lett. B **695**, 149 (2011).
[18] A. Adare et al. (PHENIX Collaboration), Phys. Rev. D **82**, 012001 (2010).
[19] A. Abulencia et al. (CDF Collaboration), Phys. Rev. Lett. **99**, 132001 (2007).
[20] M. Butenschön and B. A. Kniehl, Phys. Rev. Lett. **106**, 022003 (2011).
[21] D. Acosta et al. (CDF Collaboration), Phys. Rev. D **71**, 032001 (2005).
[22] C. Adloff et al. (H1 Collaboration), Eur. Phys. J. C **25**, 25 (2002).
[23] F. D. Aaron et al. (H1 Collaboration), Eur. Phys. J. C **68**, 401 (2010).
[24] Y.-Q. Ma, K. Wang, and K.-T. Chao, Phys. Rev. Lett. **106**, 042002 (2011).
[25] B. Gong, X. Q. Li, and J.-X. Wang, Phys. Lett. B **673**, 197 (2009), ISSN 0370-2693.
[26] A. Adare et al. (PHENIX Collaboration), Phys. Rev. Lett. **107**, 142301 (2011).
[27] A. Adare et al. (PHENIX Collaboration), Phys. Rev. C **84**, 054912 (2011).
[28] A. Adare et al. (PHENIX Collaboration), Phys. Rev. Lett. **98**, 232301 (2007).
[29] K. Adcox et al. (PHENIX Collaboration), Nucl. Instrum. Meth. A **499**, 469 (2003).
[30] K. Adcox et al. (PHENIX Collaboration), Nucl. Instrum. Meth. A **499**, 489 (2003).
[31] J. T. Mitchell et al. (PHENIX Collaboration), Nucl. Instrum. Meth. A **482**, 491 (2002).
[32] H. Akikawa et al. (PHENIX Collaboration), Nucl. Instrum. Meth. A **499**, 537 (2003).
[33] M. Allen et al. (PHENIX Collaboration), Nucl. Instrum. Meth. A **499**, 549 (2003).
[34] S. S. Adler et al. (PHENIX Collaboration), Phys. Rev. Lett. **91**, 241803 (2003).
[35] A. Adare et al. (PHENIX Collaboration), Phys. Rev. C **84**, 044905 (2011).
[36] A. Adare et al. (PHENIX Collaboration), Phys. Rev. C **81**, 034911 (2010).
[37] W. Vogelsang (2007), private communication.
[38] A. Spiridonov, hep-ex/0510076 (2004).
[39] A. Adare et al. (PHENIX Collaboration), Phys. Rev. Lett. **97**, 252002 (2006).
[40] A. Adare et al. (PHENIX Collaboration), Phys. Rev. Lett. **103**, 082002 (2009).
[41] M. M. Aggarwal et al. (STAR Collaboration), Phys. Rev. Lett. **105**, 202301 (2010).
[42] T. Sjostrand, S. Mrenna, and P. Skands, JHEP **05**, 026 (2006).
[43] E. Norrbin and T. Sjostrand, Eur. Phys. J. C **17**, 137 (2000).
[44] J. Pumplin et al. (CTEQ6M), JHEP **07**, 012 (2002).
[45] GEANT *3.2.1*, CERN Computing Library (1993), `http://wwwasdoc.web.cern.ch/wwwasdoc/pdfdir/geant.pdf`.
[46] A. Adare et al. (PHENIX Collaboration), Phys. Lett. B **670**, 313 (2009).
[47] T. A. Armstrong et al. (E760 Collaboration), Phys. Rev. D **54**, 7067 (1996).
[48] C. Amsler et al. (Particle Data Group Collaboration), Phys. Lett. B **667**, 1 (2010).
[49] L. Aphecetche et al. (PHENIX Collaboration), Nucl. Instrum. Meth. A **499**, 521 (2003).
[50] K. Sridhar, Phys. Rev. Lett. **70**, 1747 (1993).
[51] F. Cooper, M. X. Liu, and G. C. Nayak, Phys. Rev. Lett. **93**, 171801 (2004).
[52] A. D. Frawley, T. Ullrich, and R. Vogt, Phys. Rept. **462**, 125 (2008).
[53] R. Vogt (2009), private communication.
[54] M. Gluck, E. Reya, and A. Vogt (GRV98), Eur. Phys. J. C **5**, 461 (1998).
[55] A. D. Martin, R. G. Roberts, W. J. Stirling, and R. S. Thorne (MRST99), Eur. Phys. J. C **14**, 133 (2000).
[56] K. J. Anderson et al., Phys. Rev. Lett. **37**, 799 (1976).
[57] J. G. Branson et al., Phys. Rev. Lett. **38**, 1331 (1977).
[58] M. E. Binkley et al., Phys. Rev. Lett. **37**, 574 (1976).
[59] L. Antoniazzi et al. (E705 Collaboration), Phys. Rev. D **46**, 4828 (1992).
[60] E. J. Siskind et al., Phys. Rev. D **21**, 628 (1980).
[61] A. Gribushin et al. (E672 Collaboration), Phys. Rev. D **62**, 012001 (2000).

[62] T. Alexopoulos et al. (E771 Collaboration), Phys. Rev. D **55**, 3927 (1997).
[63] M. H. Schub et al. (E789 Collaboration), Phys. Rev. D **52**, 1307 (1995).
[64] C. Albajar et al. (UA1 Collaboration), Phys. Lett. B **256**, 112 (1991).
[65] B. I. Abelev et al. (STAR Collaboration), Phys. Rev. C **80**, 041902 (2009).
[66] A. G. Clark et al., Nucl. Phys. B **142**, 29 (1978).
[67] K. Adcox et al. (PHENIX Collaboration), Nucl. Phys. A **757**, 184 (2005).
[68] S. Berman, J. Bjorken, and J. B. Kogut, Phys. Rev. D **4**, 3388 (1971).
[69] R. Blankenbecler, S. J. Brodsky, and J. F. Gunion, Phys. Rev. D **12**, 3469 (1975).
[70] R. Blankenbecler, S. J. Brodsky, and J. F. Gunion, Phys. Lett. B **42**, 461 (1972).
[71] R. Cahalan, K. Geer, J. B. Kogut, and L. Susskind, Phys. Rev. D **11**, 1199 (1975).
[72] A. Adare et al. (PHENIX Collaboration), Phys. Rev. Lett. **101**, 122301 (2008).
[73] L. Antoniazzi et al. (E705 Collaboration), Phys. Rev. Lett. **70**, 383 (1993).
[74] B. Alessandro et al. (NA50 Collaboration), Eur. Phys. J. C **48**, 329 (2006).
[75] M. C. Abreu et al. (NA51 Collaboration), Phys. Lett. B **438**, 35 (1998).
[76] P. Faccioli, C. Lourenco, J. Seixas, and H. K. Woehri, JHEP **10**, 004 (2008).
[77] S. R. Hahn et al., Phys. Rev. D **30**, 671 (1984).
[78] T. Alexopoulos et al. (E771 Collaboration), Phys. Rev. D **62**, 032006 (2000).
[79] I. Abt et al. (HERA-B Collaboration), Phys. Lett. B **561**, 61 (2003).
[80] F. G. Binon et al. (Serpukhov-Brussels-Annecy(LAPP) Collaboration), Nucl. Phys. B **239**, 311 (1984).
[81] Y. Lemoigne et al., Phys. Lett. B **113**, 509 (1982).
[82] V. Koreshev et al. (E672-E706 Collaboration), Phys. Rev. Lett. **77**, 4294 (1996).
[83] C. Kourkoumelis et al., Phys. Lett. B **81**, 405 (1979).
[84] F. Abe et al. (CDF Collaboration), Phys. Rev. Lett. **79**, 578 (1997).
[85] Y.-Q. Ma, K. Wang, and K.-T. Chao, Phys. Rev. D **83**, 111503 (2011).
[86] R. Vogt, Nucl. Phys. A **700**, 539 (2002).